Abstract

TOMBAK, Ali. Radio Frequency Applications of Barium Strontium Titanate Thin Film Tunable Capacitors. (Under the supervision of Amir S. Mortazawi).

Properties of thin film barium strontium titanate (BST) based capacitors for RF and microwave components were studied. The capacitors were measured for their tunability, loss tangent, frequency dependence of dielectric permittivity, and behavior at large RF signal amplitudes. A nonlinear equivalent circuit model for tunable BST capacitors was developed.

Analysis of a tunable low pass filter fabrication using BST capacitors along with its intermodulation distortion measurements was given. Several simulations for bandpass filters were performed. Furthermore, a periodically loaded coplanar waveguide phase shifter utilizing the BST capacitors was designed.

1. REPORT DATE **2000**	2. REPORT TYPE	3. DATES COVERED **00-00-2000 to 00-00-2000**
4. TITLE AND SUBTITLE **Radio Frequency Applications of Barium Strontium Titanate Thin Film Tunable Capacitors**		5a. CONTRACT NUMBER
		5b. GRANT NUMBER
		5c. PROGRAM ELEMENT NUMBER
6. AUTHOR(S)		5d. PROJECT NUMBER
		5e. TASK NUMBER
		5f. WORK UNIT NUMBER
7. PERFORMING ORGANIZATION NAME(S) AND ADDRESS(ES) **North Carolina State University,Department of Electrical Engineering,Raleigh,NC,27695**		8. PERFORMING ORGANIZATION REPORT NUMBER
9. SPONSORING/MONITORING AGENCY NAME(S) AND ADDRESS(ES)		10. SPONSOR/MONITOR'S ACRONYM(S)
		11. SPONSOR/MONITOR'S REPORT NUMBER(S)
12. DISTRIBUTION/AVAILABILITY STATEMENT **Approved for public release; distribution unlimited**		
13. SUPPLEMENTARY NOTES **The original document contains color images.**		
14. ABSTRACT		
15. SUBJECT TERMS		

16. SECURITY CLASSIFICATION OF:			17. LIMITATION OF ABSTRACT	18. NUMBER OF PAGES **63**	19a. NAME OF RESPONSIBLE PERSON
a. REPORT **unclassified**	b. ABSTRACT **unclassified**	c. THIS PAGE **unclassified**			

RADIO FREQUENCY APPLICATIONS OF BARIUM STRONTIUM TITANATE THIN FILM TUNABLE CAPACITORS

by

ALİ TOMBAK

A thesis submitted to the Graduate Faculty of
North Carolina State University
in partial fullfilment of the
reqirements for the Degree of
Master of Science

ELECTRICAL ENGINEERING

Raleigh

2000

APPROVED BY:

_____   _____
                                          Jon-Paul Maria

_____
Chair of Advisory Committee

Dedication

This thesis is dedicated to my mother, my father and to my sister for their moral support and motivation.

Personal Biography

Ali Tombak was born in Turkey on September 20, 1977. He received his B.S. degree in Electrical and Electronics Engineering at the Middle East Technical University, Ankara, Turkey. While pursuing his B.S. degree, he worked part-time in ASELSAN (Military Electronics Company) Communication Division from February 1998 to June 1999. Upon completing his B.S. degree, he was admitted to the Electrical and Computer Engineering Department of North Carolina State University, Raleigh, NC where he held a Research Assistantship position.

Ali Tombak took the first degree in National Science Olympics on Physics which was organized by Turkish Scientific and Technical Research Council in 1993. He also took the "Assoc. Prof. Dr. Bülent Kerim Altay Award" at the Middle East Technical University in 1996.

His research interests include RF and microwave circuits in communication applications, and the integration of ferroelectric materials into RF circuits. He is a student member of the Institute of Electrical and Electronic Engineers and a member of the Microwave Theory and Techniques Society.

Acknowledgements

Contents

List of Figures

List of Tables

List of Symbols

BST   - Barium Strontium Titanate $(Ba_x, Sr_{1-x})TiO_3$.

STO   - $SrTiO_3$.

HTS   - High temperature superconductor.

MOCVD   - Metal Organic Chemical Vapor Deposition.

ADS   - Advanced Design System.

LSSP   - Large Signal S-Parameter.

HB   - Harmonic Balance.

IP3   - 3rd order intercept point.

IMD   - Intermodulation distortion.

ε_r - Relative dielectric permittivity of BST.

R_S - Series resistance.

R_P - Parallel resistance.

$\tan\delta$ - Loss tangent of the dielectric.

Q   - Quality factor of a capacitor.

x   - Loading factor of the phase shifter.

Z_i - Unloaded line characteristic impedance of the phase shifter.

υ_i - Phase velocity on the high impedance line.

$C_{var}^{\ max}$ - Zero bias capacitance for the phase shifter.

L_{sect} - Length of one unit cell of the phase shifter.

N_{sect} - Total number of sections of the phase shifter.

L_t - Inductance per unit length of the high impedance line.

C_t - Capacitance per unit length of the high impedance line.

$\Delta\vartheta$ - Phase shift per unit cell.

g_i - Prototype element values of the ith component.

ω_c - Cut-off frequency of the filter.

R_0 - Characteristic impedance of the 1st and 2nd ports.

Chapter 1

Introduction

Barium strontium titanate $(Ba_x, Sr_{1-x})TiO_3$ (BST) is a material which can exhibit paraelectric or ferroelectric properties depending upon the specific composition and temperature. The permittivity of paraelectric BST can be controlled electronically by applying a DC electric field across it. By exploiting this property of BST, tunable RF and microwave capacitors (varactors) can be fabricated [1]-[4]. In parallel plate capacitors, tunabilities greater than 50% are achievable at DC bias levels as low as 2 Volts [1]. BST varactors also offer a host of advantages. These include the ease of integration with active devices such as MMICs, low cost simultaneous fabrication of multiple parts, low losses in high quality films, and minimal frequency dispersion. In addition, tunable BST capacitors do not produce junction noise (as compared to varactor diodes), and due to the high dielectric constant of BST thin films (typically around 300) [5], very high energy density capacitors can be fabricated on appropriately buffered Si substrates.

A voltage controlled capacitor is one of the core components in tunable RF and microwave devices, such as voltage controlled oscillators (VCO), tunable filters, phase shifters, and tunable matching networks. BST varactors seem to be a great candidate for the construction of adaptive communication systems, in both commercial and military applications with the ability to adapt to various conditions (such as temperature, noise, fading etc…) for optimum operation. The motivation behind this work was the integration of BST varactors into these applications. This integration requires detailed characterization of the frequency and the field dependence of both the permittivity

(tunability) and the dielectric loss tangent (tanδ) of BST. Accurate measurements of BST up to microwave frequencies must be performed to achieve these goals.

The tasks undertaken here can be divided into three parts. The first is to characterize the RF and microwave properties of the BST capacitors, and to understand their behavior under large RF signal excitation. The second task is the design and fabrication of tunable filters, and the characterization of the intermodulation distortion introduced by the BST capacitors. Lastly, the required properties of the BST capacitors and the conductor for the design of low loss tunable phase shifters must be investigated.

1.1. Thesis Overview

Chapter 2 presents a review of the previously published work on BST including fabrication process, measurement results for BST capacitors, and several applications including phase shifters and tunable filters. Chapter 3 describes the fabrication process used to grow BST thin films in this work, and gives the detailed material information.

Chapter 4 discusses the measurement setup and results for the BST capacitors at RF and microwave frequencies. The large signal measurement results are also included in chapter 4.

In chapter 5, the design of tunable lowpass and bandpass filters and the implementation of a tunable low pass filter are presented. Chapter 6 covers a periodically loaded distributed phase shifter design, and discusses the main requirements for a BST capacitor in this application. Finally, in chapter 7, conclusions and suggestions for future work are discussed.

Chapter 2

Literature Review

2.1. Introduction

Ferroelectric thin films are very promising for the design of a wide range of devices such as high dielectric capacitors, non-volatile memories with low switching voltage, infrared sensors and electro-optic devices [6]. They have a characteristic temperature - the transition temperature T_C – at which the material makes a structural phase change from a polar phase (ferroelectric) to a non-polar phase (paraelectric). The ferroelectric phase possesses an equilibrium spontaneous polarization that can be reoriented by an applied electric field. The culmination of this field response is best observed in a polarization field hysteresis loop. At the characteristic temperature T_C, the material changes from the ferroelectric phase to the paraelectric phase, in which the spontaneous polarization equals zero, however the relative dielectric constant (ε_r) remains large and can be changed with the applied electric field. Materials in the ferroelectric phase exhibit a hysteresis, which is absent in the paraelectric phase. Hence, the ferroelectric phase is preferred in non-volatile memory applications, whereas the paraelectric phase is preferred for dynamic random accessible memories (DRAM) [7].

Among the great variety of ferroelectric compositions, two families of materials have emerged. These are the lead titanate family of solid solutions including PZT and PLZT, and the barium strontium titanate solid solution family which includes several

paraelectric phase materials such as (Ba,Sr)TiO$_3$ (BST) (where Ba/Sr < 70% at room temperature) [7]. It should be noted that a large array of ferroelectric and paraelectric materials exists, however, in general, the majority of their properties are represented by the two families mentioned.

Due to the negligible frequency dependence and high dielectric constant of well prepared BST compositions, significant attention has been given to these materials for a variety of novel applications. This is mainly because, BST allows the construction of small cell size and large-scale DRAMs [7]. Also, the nonlinear dielectric properties of these ferroelectric films with respect to the applied DC bias enables the fabrication of electronically tunable capacitors. Therefore, these capacitors can be used to construct tunable microwave devices, such as voltage controlled oscillators (VCO), tunable filters, phase shifters, tunable matching networks, and frequency multipliers.

Currently, varactor diodes are extensively used in most of the RFIC applications including voltage-controlled oscillators, tunable filters and phase shifters. However, they suffer from high losses at microwave frequencies, and their quality factor drops exponentially when the frequency approaches to 1-2 GHz [18], [19]. Other drawbacks of varactor diodes are the junction noise resulting from the electron/hole collisions and relatively high tuning voltages.

Tunable devices employing ferroelectric thin films have the potential to achieve fast tuning speeds, low microwave losses, low drive powers and potentially low costs [8]. For modern microwave integrated microelectronics, the use of thin film ferroelectric films is preferable to bulk elements [8]. However, there does not seem to be a standard or best method of deposition of thin films. Among different techniques studied, chemical vapor deposition (CVD) is usually considered to be the most promising one. It has several advantages such as excellent composition control, large area coverage, and the

potential for areal homogeneity and conformal coating of complicated topography [7], [9], [10].

So far, research activities to characterize the microwave properties of these materials primarily include the use of high temperature superconductors (HTS e.g. YBCO) on pure $SrTiO_3$ (STO) dielectric layers. In most cases, an interdigitated capacitor or a microstrip resonator is fabricated. From the measured quality factor and the resonant frequency, the loss tangent, the relative dielectric constant and the tunability of the STO thin films are extracted. Table 2.1 below summarizes the measurement results of several recent studies.

Table 2.1: A summary of the past measurement results for STO thin films.

	Tunability	Loss tangent $(\tan\delta)$ at $77K^o$
Raymond [11]	2.5:1	0.003 at 10 kHz, 0.01 at 1-2 GHz
Kozyrev [12], [13]	1.6:1	0.03-0.05 at 3 GHz
Galt [14]	2.0:1	0.01 at 6-20 GHz
Treece [15]	2.25:1	0.01 at 1 MHz

The devices presented in [11]-[15] employed high temperature superconductors and were generally based on planar structures which required very high tuning voltages and temperatures below 90K for optimal operation. The STO thin films show non-tunable characteristics at room temperature [15]. For room temperature applications, BST thin films are preferred. Tunabilities greater than 50% are achievable in parallel plate capacitors with the application of DC bias levels ranging from 2 to 5 volts (thickness $\cong$ 700 A^o) [1]. Also, loss tangents as low as 0.002 at kHz range frequencies have been achieved [16]. Table 2.2 summarizes the current status of BST thin films.

Table 2.2: Current status of BST thin films.

	Tunability	**Loss tangent (tanδ)**
Pond [17]	1.7:1	0.02 at UHF
Stauf [16]	N/A	0.002 at kHz range frequencies
Tombak [1]	2.4:1	0.004 at VHF frequencies

Currently, a significant amount of research is being conducted to improve the properties of BST capacitors and to incorporate them into the RF and microwave devices mentioned above. This integration requires detailed characterization of the frequency and the field dependence of both permittivity (tunability) and dielectric loss tangent (tanδ) of the BST at RF and microwave frequencies.

2.2. Applications of BST in Tunable RF/Microwave Devices

It was previously mentioned that BST is one of the promising candidates for the construction of high frequency tunable filters and phase shifters. In this section, a brief review of ferroelectric tunable filters and phase shifters is given.

2.2.1 Tunable Filters

Field dependent dielectric constant of BST can be exploited for RF and microwave tunable filter applications. Planar microstrip HTS tunable filters are currently being tested by the wireless industry for low-loss high performance receiver front-end systems. Initial applications have been successful [20].

A two-pole tunable bandpass filter was designed by Subramanyam using microstrip-edge coupled resonators [21]. STO thin films were deposited on LaAlO$_3$ by Laser Ablation Technique and YBCO thin films were used as metallization. The filter operated at a center frequency of 17.4 GHz, and yielded 9% tunability with the application of +/- 500V at 77K. The insertion loss (IL) of the filter was better than 3.3 dB

and the return loss (RL) was also higher than 10 dB at 77K. This result of IL and tunability compares better with a similar study [20], and seems to be promising for satellite communication applications. The STO thin films had loss tangent values ranging from 0.005 to 0.05 at GHz frequencies.

An important parameter to assess the dynamic range of a tunable filter is the level of spurious signal generated by the varactors in the filter. Third order intermodulation distortion (IMD) products are generated when two fundamental signals of frequencies, f_1 and f_2, which are close to each other, are applied to nonlinear devices. The third order IMD frequencies are given by $f_{IMD}=2f_1-f_2$, and $f_{IMD}=2f_2-f_1$. The difference in power levels between the fundamental and the third order IMD signal determines the maximum dynamic range of microwave circuits, thus this difference must be optimized for maximum circuit performance.

In [13], the intermodulation distortion measurements were made on a microstrip resonator which uses STO capacitors. The intermodulation data showed that the level of the 3rd order products is at least 15 dB below the fundamental signal, thus this shows that the power handling capability of these capacitors are much higher than contemporary varactors diodes.

The tunable bandpass filters discussed in [20] and [21] utilized high temperature superconductors and planar structures, and thus required very low temperatures for optimum operation and tuning voltages of several hundred volts. Therefore, it is very difficult to incorporate them into low cost RF components at room temperature. On the other hand, the BST capacitors described in [1] are promising for the design of low loss, low cost and high performance tunable circuits. They can also be integrated with active devices [5], [16].

2.2.2 BST Phase Shifters

One of the important applications of BST is electronically controlled phase shifters. Currently, most of the phased array antenna systems rely on ferrite and semiconductor based phase shifters. Ferrite phase shifters are very slow to respond to control voltages. Semiconductor based phase shifters are much faster, but they suffer from high losses at microwave frequencies and have limited power handling capabilities [22]. At this point, ferroelectric materials offer a variety of benefits to overcome these difficulties. A ferroelectric based phase shifter operates by changing the phase velocity of a guiding structure through a change in the permittivity of the dielectric.

A loaded line phase shifter, which utilizes thin film ferroelectric capacitors to periodically load a high impedance transmission line is reported in [22], [23]. Fig.2.1 shows the schematic representation of the phase shifter.
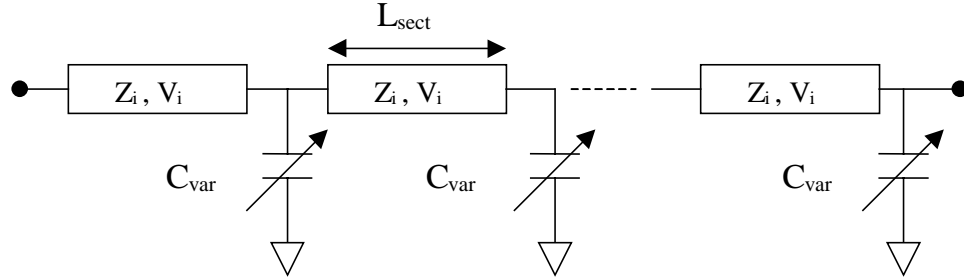
Figure 2.1: Circuit schematic of the phase shifter.

This structure behaves like a synthetic transmission line and can be approximated in terms of the inductance and the capacitance per unit length of the transmission line at frequencies much lower than the cut-off frequency (Bragg frequency) that the approximate circuit represents [23]. The insertion of BST capacitors does not change the inductance per unit length. The characteristic impedance and the phase velocity of the transmission line are both changed by applying a voltage to the BST capacitors. Based upon the tuning ratio of the BST capacitors, phase shift per unit cell can be calculated. It is desirable for the characteristic impedance of the loaded transmission line to be 50 Ω

for impedance matching purposes, so it is important to have precise line dimensions and substrate properties for the transmission line.

Erker et al. has demonstrated a Ka-Band phase shifter using BST parallel plate capacitors [22]. A transmission line (coplanar waveguide, CPW) of characteristic impedance 100 Ω on a high resistivity silicon substrate (40 kΩ-cm) was fabricated. The CPW line was loaded by BST capacitors with a zero bias capacitance of 96 fF. The section length of one unit cell was chosen as 340 μm. The phase shifter was designed to produce 160° phase shift at 20 GHz, thus requiring 9 identical cells to be connected in series. A phase shift of 157° at 30 GHz with an insertion loss of 5.8 dB was reported. The measured return loss was higher than 12 dB. The performance of the periodically loaded distributed phase shifters will improve further when low loss BST thin films are utilized [22].

In the following chapters, the material properties and the approach to characterize the loss tangent and tunability of the BST capacitors will be discussed. Finally, implementation of the BST capacitors into the above applications will be studied.

Chapter 3

Material Properties and Fabrication

The BST thin films used in this project have been grown in Advanced Technology Materials Inc., in Danbury, CT USA. Top metallization was depozited in the Materials Science and Engineering Department at North Carolina State University, Raleigh, NC USA. This chapter is intended to give some material and fabrication information of the BST capacitors.

Parallel plate capacitors for this project were fabricated on 500 µm thick silicon wafers covered with approximately 500 Å of thermal SiO_2 and a final 1000 Å of Pt (this Pt layer acts as the device ground plane – see Fig.3). $(Ba_{0.7}Sr_{0.3})TiO_3$ was grown by metalorganic chemical vapor deposition to thicknesses between 500 and 5000 Å. MOCVD is the deposition method of choice for the fabrication of BST thin films. It provides excellent composition control, large area coverage, and the potential for areal homogeneity and conformal coating of complicated topography [9], [24]. In this work, all BST films were uniformly deposited on 150 mm wafers, thus indicating the suitability for commercial mass production. Top electrodes completing the parallel plate capacitor structures were deposited by either sputtering or electron-beam evaporation. Using standard photolithographic methods and reactive ion etching, the top platinum surface was patterned. To achieve the best electrical properties, it was necessary to anneal the top electrodes after deposition at 550 °C for 30 minutes in air. This annealing process results in reduced loss tangents and reduced dielectric dispersion. If samples are re-exposed to atmosphere for extended periods after this annealing step, in order to maintain reliable

electrical properties, this step must be repeated. It is believed that atmospheric moisture will in some way influence the film/electrode interface over time and degrade the interfacial electrical properties. This implies that BST components in real circuits must be capped with layers providing isolation.

Structural characterization was performed to assess the quality of the BST films. X-ray diffraction and atomic force microscopy were used to determine the crystal structure and surface roughness, respectively. Figure 3.1 shows a typical x-ray diffraction pattern of the BST films used in this study.
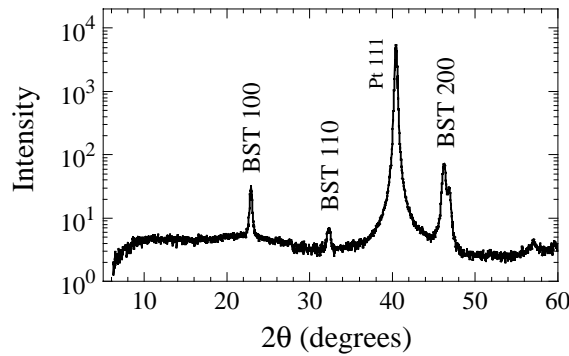
Figure 3.1: Xrd pattern for a typical BST thin film.

This pattern indicates that the material is perovskite single phase with good crystal quality. In addition, the relative peak intensities indicate that a bimodal distribution of (110) and (001) orientations is present. In most cases, however, the (001) oriented fraction is predominant. This type of spectrum is typical of high quality BST material and can be reproduced over many deposition cycles [25]. Figure 3.2 is an atomic force microscope (AFM) (non-contact) image of a BST thin film surface. This image is typical of BST thin films in the thickness range between 500 Å and 2000 Å. The surface image indicates a uniform microstructure with a surface grain size of approximately 80 nm. In addition, a surface roughness of approximately 5 nm rms is indicated.
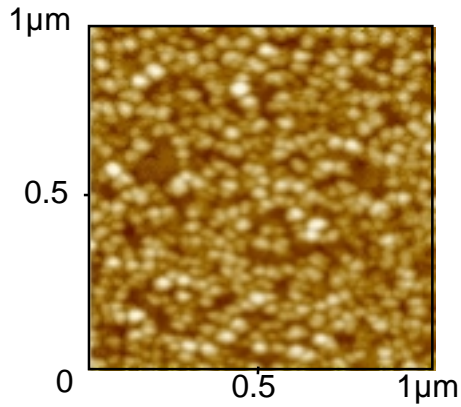
Figure 3.2: AFM image of typical BST thin film.

From the previous work on BST thin films, the importance of the composition in producing the ultra-low loss material was recognized and well understood [9]. The results clearly show that compositions containing a small titanium (Ti) excess lead to the lowest loss tangent values. The Ti excess will also result in reduced permittivities, but the effect on capacitance density can be easily compensated by reducing the film thickness. The samples used in our experiments have a Ti excess of approximately 2.5%. Measurements of composition were made using a grazing incidence x-ray fluorescence technique. In all cases, the Ba/Sr ratio used was about 70/30 [26]. This composition was chosen since it provides a material with a high permittivity and tunability at room temperature. In addition, the 70/30 composition corresponds to a material which is paraelectric at room temperature, thus will provide a non-hysteric voltage response.

Chapter 4

Measurements of BST Capacitors

4.1. Introduction

The integration of BST thin films with the RF and microwave applications mentioned so far requires detailed characterization of the frequency and the field dependency of both the permittivity (tunability) and the dielectric loss tangent (tanδ) of BST. Accurate measurements of BST up to microwave frequencies must be performed to achieve these goals.

In this chapter, measurements, modeling and characterization of the BST capacitors will be described. Furthermore, measured results for frequency dependent permittivity and tunability at large RF signal amplitudes will be presented.

4.2. BST Tunable Capacitor Measurements and Modeling

An HP8510C Vector Network Analyzer was used to characterize the small signal impedance of the parallel plate BST capacitors based on the measurement setup in Figure 4.1. GGB Industries' Model 10 and Model 40A high frequency probes were used to measure the capacitors. Cascade Microtech's calibration standards were used to make a one-port short-open-load (SOL) calibration at the network analyzer. Access to the ground plane was achieved through etching the BST. Figure 4.2 shows a typical contact for BST capacitors. BST capacitors having dimensions of 50 μm x 50 μm were measured at a

frequency range between 45 MHz and 1 GHz. The upper frequency limit was set by the value of the capacitance. DC bias was applied to the capacitors through a bias-tee.
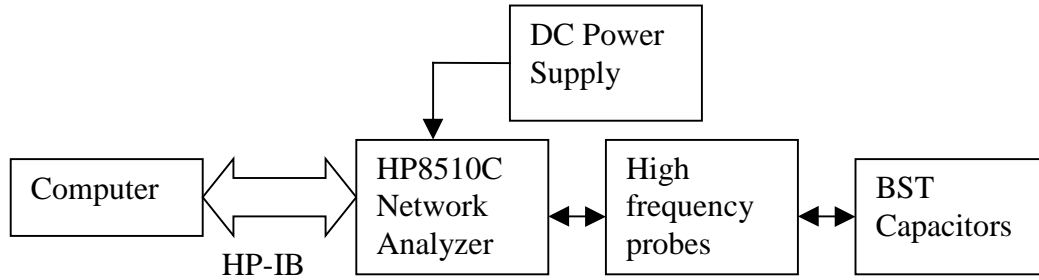
Figure 4.1: Small signal measurement setup.
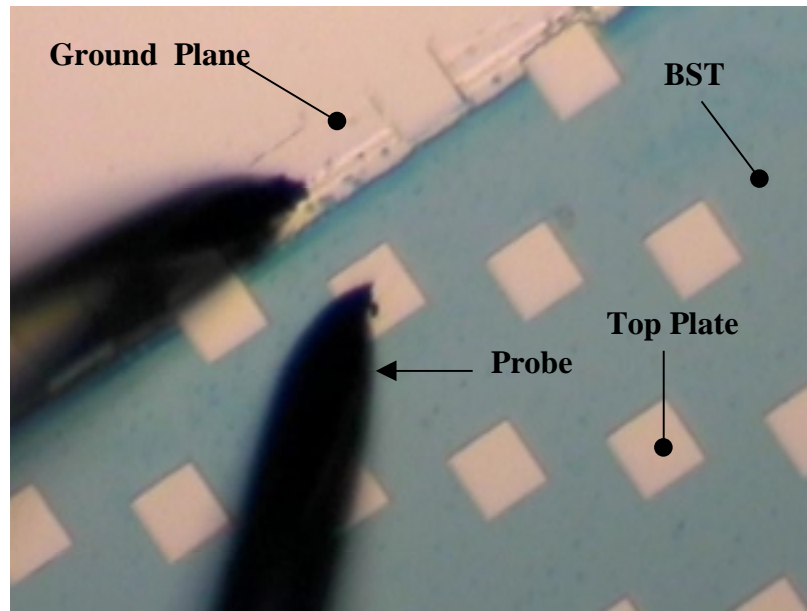
Figure 4.2: A typical probe contact for the BST capacitors.

To extract the loss tangent and dielectric constant of BST, the capacitors were modeled as shown in Figure 4.3. In this model, the series resistor, R_S, is used to account for the losses due to probe contacts and conductor losses, while the shunt resistor, R_P, accounts for the BST losses ($\tan\delta$).
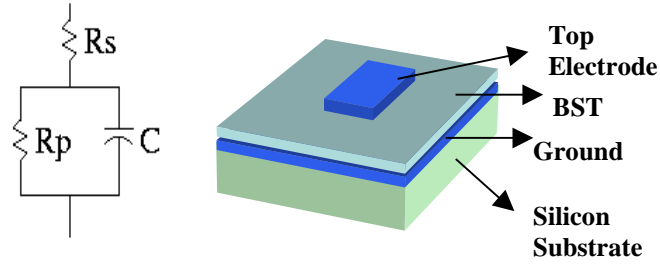
Figure 4.3: Schematic illustration of a planar BST thin film capacitor with Pt electrodes and the associated circuit used to model the electrical data.

The model parameters in Figure 4.3 were optimized in HP-Advanced Design System (ADS) simulation program to achieve the best fit to the measured reflection coefficients over a given frequency range. The simulation setup is shown in Appendix A.

Several BST parallel plate capacitors were measured to characterize the dielectric constant and loss tangent of BST. The measured data was optimized within the frequency range from 45 MHz to 200 MHz to yield unique solutions for R_S, ε_r and $\tan\delta$ given in the circuit model of Figure 4.3. The graphs below (Figure 4.4-Figure 4.9) summarize the measurement results for selected samples, whose properties are shown in Table 4.1.

Table 4.1: Properties of the measured samples

Sample Name	BST Thickness (A^{o})	Platinum Thickness (A^{o})	Capacitance (pF)
AV30	703	971	59
AV48	695	975	66
AV60	666	937	61
AV62	714	931	88
AV63	735	930	87
AV68	700	938	63
AV69	722	933	61
AV175	3000	3000	31
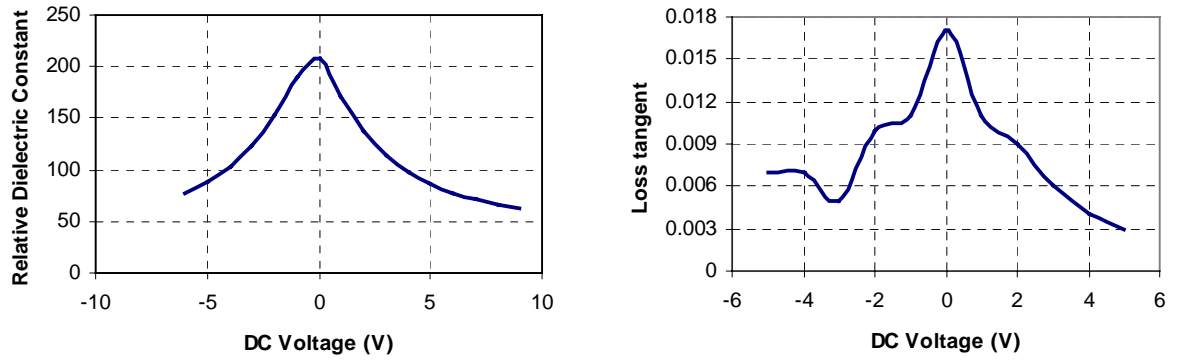
Figure 4.4: Measurement results for the sample AV48.
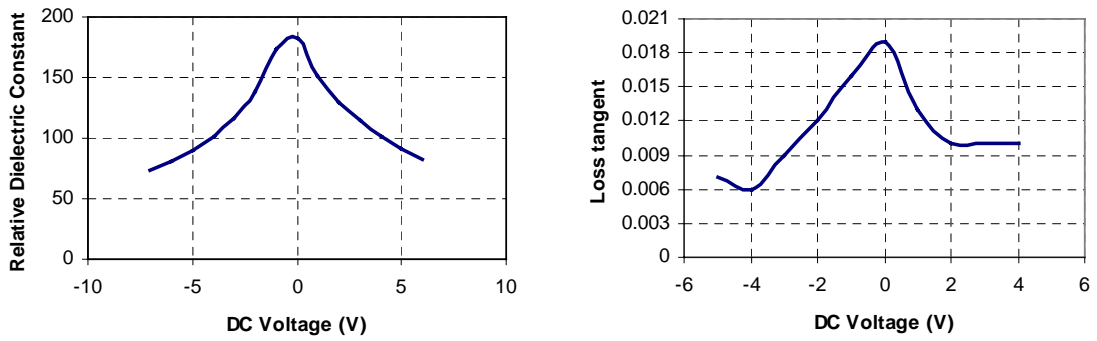
Figure 4.5: Measurement results for the sample AV60.
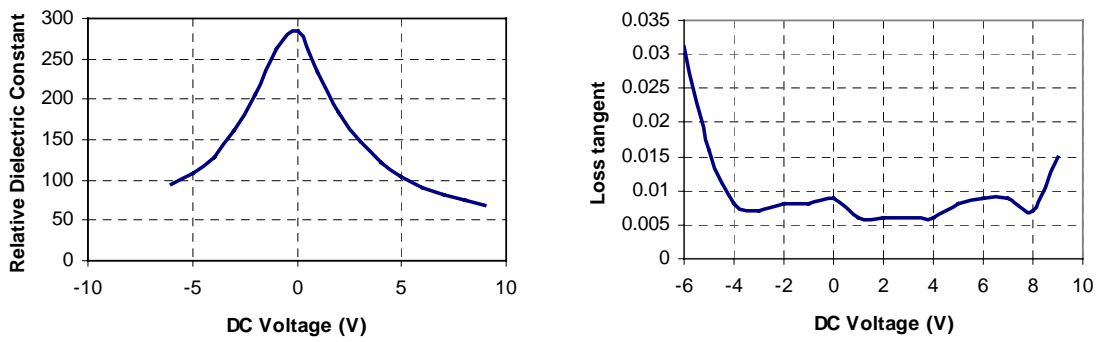
Figure 4.6: Measurement results for the sample AV62.
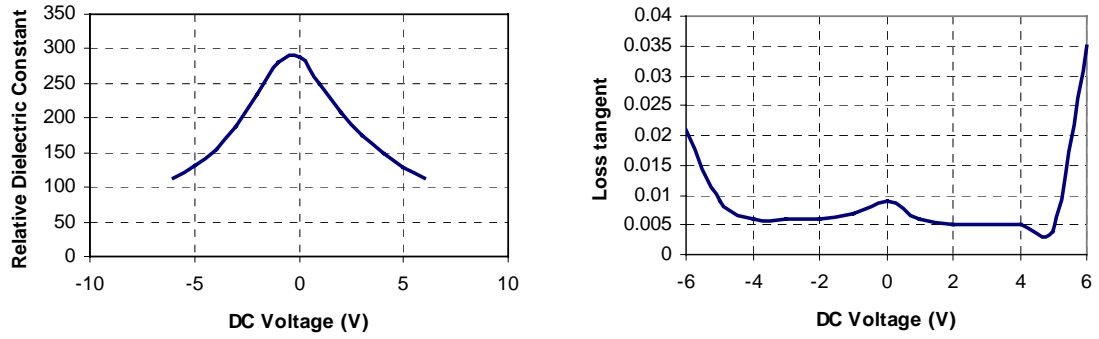
Figure 4.7: Measurement results for the sample AV63.
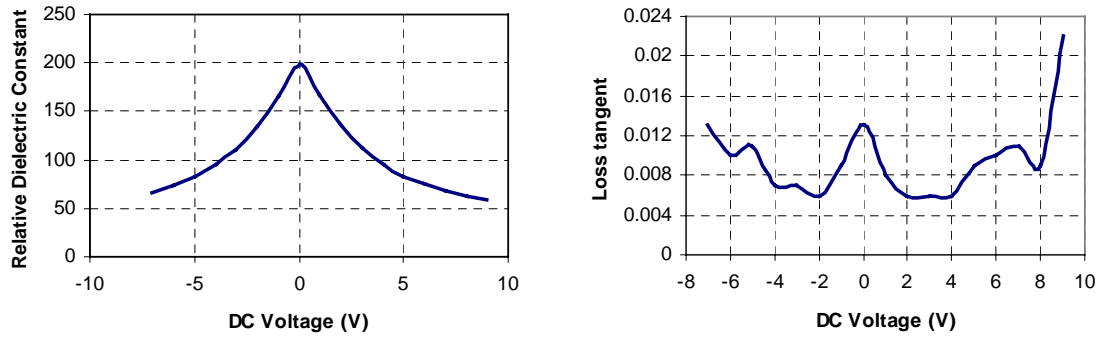
Figure 4.8: Measurement results for the sample AV68.
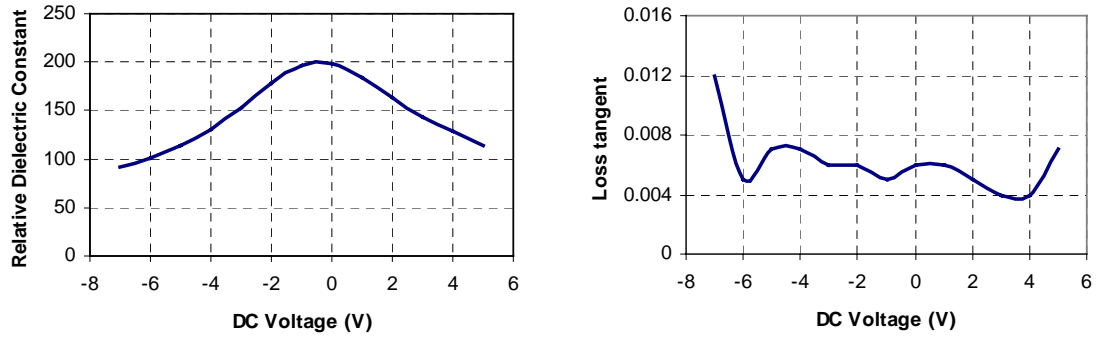
Figure 4.9: Measurement results for the sample AV69.

From these measurement results, it can be seen that tunabilities as high as 4.18:1 (76%) and loss tangents as low as 0.003 are obtainable. These losses correlate with relaxation currents in the films. The microstructural origin of these relaxation currents are

still under debate, but appear to be related to structural defects associated with the relatively low processing temperatures. It can also be seen that BST has symmetric tunability characteristics around 0 V, and the loss tangent of the material drops when DC bias is applied.

An important parameter to be mentioned here is the quality factor of the measured capacitors. Total quality factor of a capacitor can be calculated using the formula below;

$$Q_{total} = \frac{imag(Z)}{real(Z)} \qquad (4.1),$$

where Z is the impedance seen from the capacitor.

The quality factors of the BST capacitors in this work were measured using an HP8510C Network Analyzer. The measured S-parameters were converted to Z-parameters and the formula in (4.1) was applied. In Figure 4.10, the total quality factor of a typical BST capacitor can be seen. The obtained quality factor is already comparable with a commercially available semiconductor based varactor diode, MA-COM part #MA4ST079 tuning varactor with Q of approximately 80 at 50 MHz. It is expected that the quality factor of the BST capacitors will improve further by reducing the conductor losses.
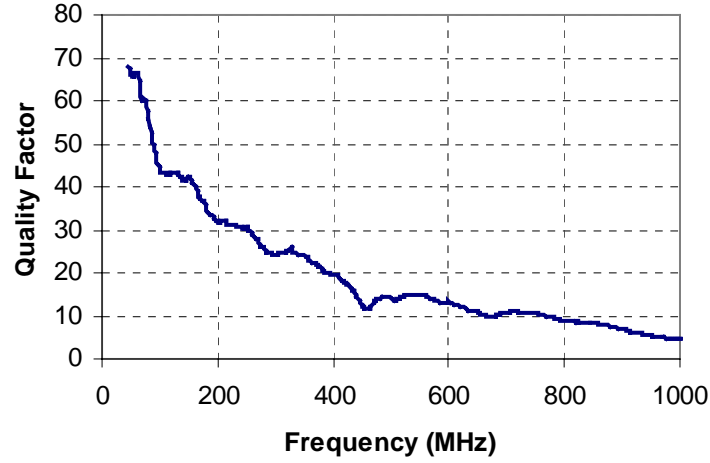
Figure 4.10: The total quality factor of a 31 pF capacitor at 0 Volt DC bias (AV175).

4.3. High Frequency Measurements

Incorporating the BST into tunable microwave applications requires the characterization of its permittivity and loss tangent at microwave frequencies. A smaller size capacitor of 20x20 μm^2 was measured up to 11 GHz using the setup in Figure 4.1. This upper frequency limit was due to the capacitance of the 20x20 μm^2 capacitors. The frequency spectrum was divided into small ranges, and the measured data was optimized for these ranges, e.g. from 45 MHz to 500 MHz, from 500 MHz to 1 GHz, and so on. The relative dielectric constant vs. frequency graph is shown in Figure 4.11. It can be seen from the graph that the dielectric permittivity is nearly constant up to microwave frequencies, introducing only 4.4 % dielectric dispersion per decade, which is similar to the values obtained [27].

A reliable loss tangent figure could not be obtained in this experiment because of the relatively poor probe contact and noisy data. However, it will be possible to measure the loss tangent by measuring a capacitor which has a more proper structure for probe

placement, e.g. a capacitor fed through a coplanar waveguide (CPW). Research on overcoming this difficulty is still underway.
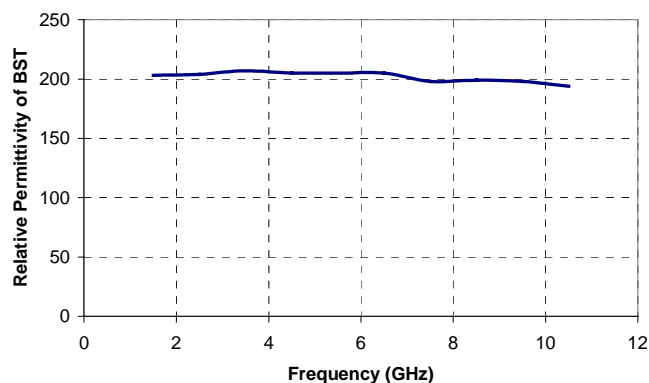
Figure 4.11: Relative dielectric permittivity of thin film BST as a function of frequency.

4.4. Large Signal Measurements and Simulations

One of the applications of BST based tunable filters and phase shifters is in transmitters, where these devices are exposed to a large amount of RF power. This requires understanding the behavior of the BST based capacitors at large RF signal amplitudes. The set-up in Figure 4.12 was established to measure the large signal behavior of BST capacitors.
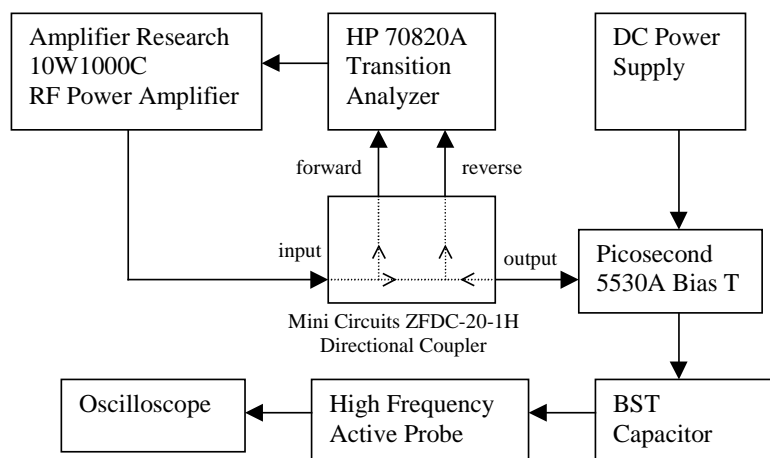
Figure 4.12: Large signal measurement set-up.

In this set-up, an HP70820A microwave transition analyzer is used to measure the large signal S-parameters of the BST capacitors. The signal generated from the source of the transition analyzer is fed into a power amplifier, and the amplified signal is fed to the directional coupler. The directional coupler couples -20 dB of the input power to the 2nd port of the transition analyzer. However, most of the power is applied to the device under test through a bias-tee. The reflected signal from the capacitor is injected to the reverse port of the transition analyzer. A calibration algorithm was written to the transition analyzer to correct for the measurement errors within the system. The details of this calibration algorithm are explained in Appendix B.

A *Model 34A-4-35* high impedance active probe with a tungsten tip was used to measure the true RF voltage amplitude across the capacitors. The probe was connected to the top plate of the capacitors while being excited with the RF signal. The voltage waveforms were observed on a high frequency oscilloscope, and the rms values of the waveforms were recorded at various RF power levels.

Figure 4.13 shows a plot of the relative permittivity as a function of the applied DC voltage for various RF signal amplitudes. The previously measured DC breakdown voltage of 8 Volts for this particular sample limited the application of higher DC voltages when high RF voltage levels were applied.
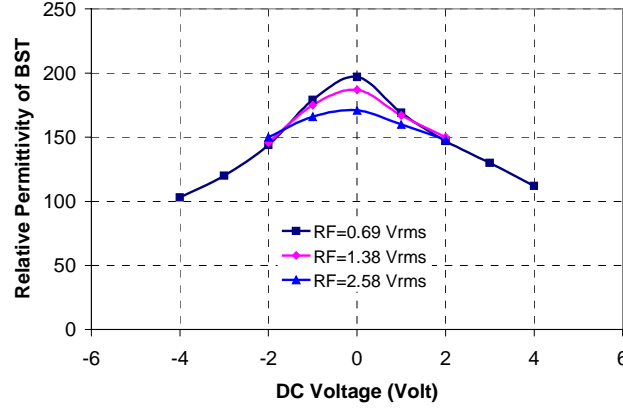
Figure 4.13: Measured relative permittivity of BST at high RF voltages (f=50 MHz, Thickness=700Å).

It can be seen that the dielectric tunability decreases with increasing the RF signal amplitude. It is suggested that the tunability drop is proportional to the rms value of the RF signal amplitude. The small signal tunability curve of this BST capacitor (Figure 4.14) was fit to a 14th order polynomial, which was then used in the nonlinear capacitor model of HP-ADS. Through a *Large Signal S-Parameter* simulation in HP-ADS, predicted results for the tunability at large RF signal amplitudes were obtained (Figure 4.15). The MATLAB program for curvefitting and the simulation setup can be seen in Appendix C and Appendix D, respectively. The results obtained from this simulation are in good agreement with the measured results. Almost the same tunability drops from the measurements and the simulations are observed. The small discrepancy in peak dielectric constants is due to imperfect curvefitting of the BST's tunability to the polynomial.

Through these measurements, it was observed that tunability of the BST capacitors drops at large RF signal levels. This effect has to be taken into account if BST is intended to be utilized in some tunable RF and microwave applications such as tunable filters, phase shifters, which are exposed to large RF signal amplitudes. The study characterizing the large signal effects was the first study made among similar research

activities. Furthermore, a nonlinear circuit model was developed, which will be important in predicting the intermodulation distortion generated by these capacitors in the RF and microwave applications mentioned. Understanding other nonlinearities in BST is still underway.
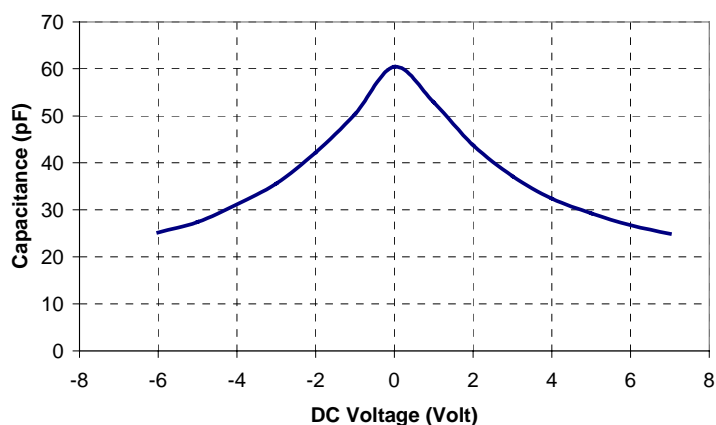
Figure 4.14: Small signal tunability curve of AV30.
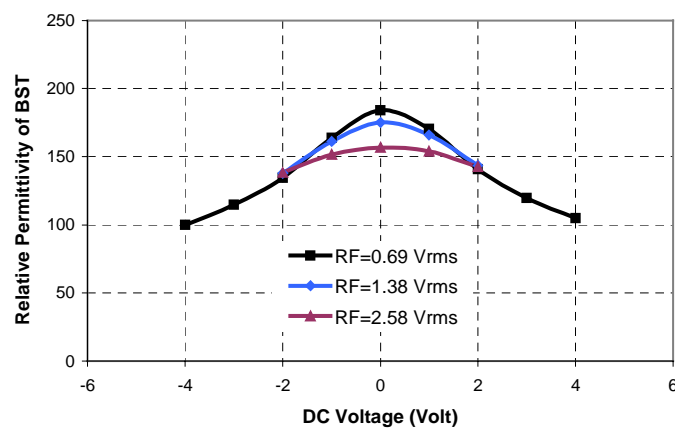
Figure 4.15: Simulated relative permittivity of the BST capacitor at measured values of RF voltages (AV30).

Chapter 5

Tunable Filters

5.1. Introduction

Tunable filters are widely used in most military applications and satellite communication systems as receiver front-ends. Most of today's tunable filters rely on either mechanical tuning or utilization of semiconductor based varactors. Mechanically tunable filters have high power handling capability with a low insertion loss. The main disadvantages of these filters are low tuning speeds, large size and mass. Semiconductor based tunable filters are much faster, but they have low power handling capabilities [28]. On the other hand, utilization of the BST capacitors offers several benefits to overcome these difficulties. In this chapter, a design approach for BST based tunable lowpass and bandpass filters will be presented. Based on the methodology given, an implemented tunable lowpass filter will be demonstrated and its intermodulation distortion measurement results along with the predicted values from simulations will be shown.

5.2. Tunable Lowpass Filters

A BST lowpass filter (LPF) can be designed using a Chebychev lowpass filter design procedure (Figure 5.1). For a given ripple (insertion loss) in the passband, the component values after frequency and impedance scaling are:

$$C = \frac{g_1}{R_0 \cdot \omega_C} \quad (5.1),$$

and

$$L = \frac{g_2 \cdot R_0}{\omega_C} \quad (5.2),$$

where g_1 and g_2 are the prototype element values from the design table, R_0 is characteristic impedance of the 1st and 2nd ports, and ω_c is the cut-off frequency of the filter [29].
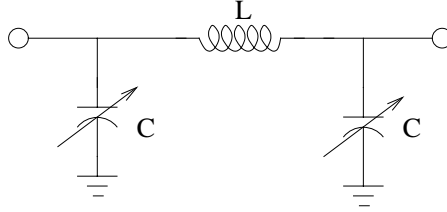
Figure 5.1: The circuit schematics of the tunable low pass filter.

Based on the measurement results from several samples, a 3rd order 0.5 dB ripple Chebychev filter with C=32 pF, and L=56 nH was designed. To build the designed filter, a microstrip fixture was used. The ground planes of the BST capacitors and the fixture were connected using silver epoxy, and the BST capacitors were connected to the signal path of the fixture by wire bonding. The designed filter including all losses from the finite Q inductors and bond wires was simulated in HP-ADS. The insertion loss and the return loss of both the simulated and measured filter responses can be seen in Figure 5.2 and Figure 5.3, respectively.

As shown in Figure 5.2, the simulated filter has a 3 dB cut-off frequency at 171 MHz, which can be tuned up to 236 MHz by halving the BST capacitors, thus resulting in a 38 % tunability. The maximum insertion loss in the passband is 0.73 dB, and the passband return loss is better than 10 dB for all bias levels. The measurement results show that the 3 dB cut-off frequency can be tuned from 160 MHz to 210 MHz by biasing the capacitors at +/- 9 V, giving 30 % tunability. Also, the maximum measured insertion loss in the passband was 0.8 dB, showing that most of the passband insertion loss comes

from the bond wires and the finite quality factor of the inductors. For all biasing conditions, the return loss in the passband was higher than 10 dB. The stopband attenuation of the filter can be further improved by designing higher order filters. The simulated and measured results are in very good agreement.
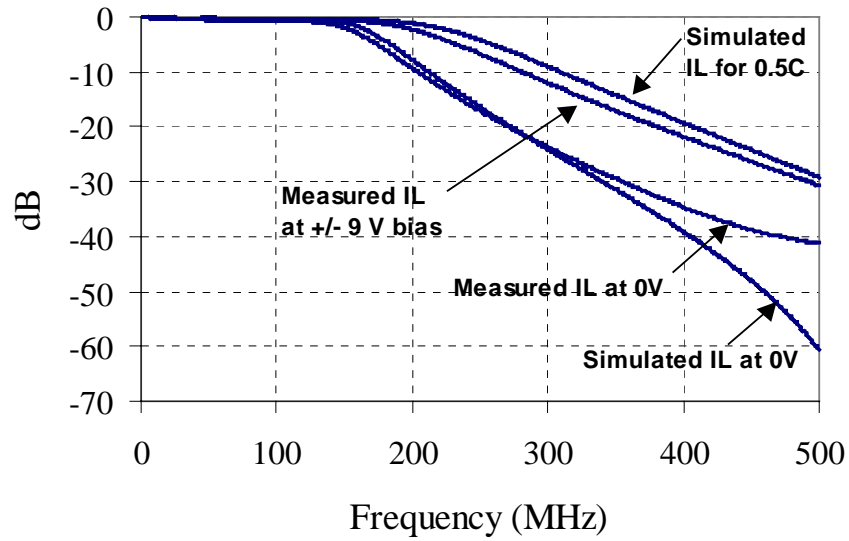
Figure 5.2: Simulated and measured insertion loss of the tunable LPF.
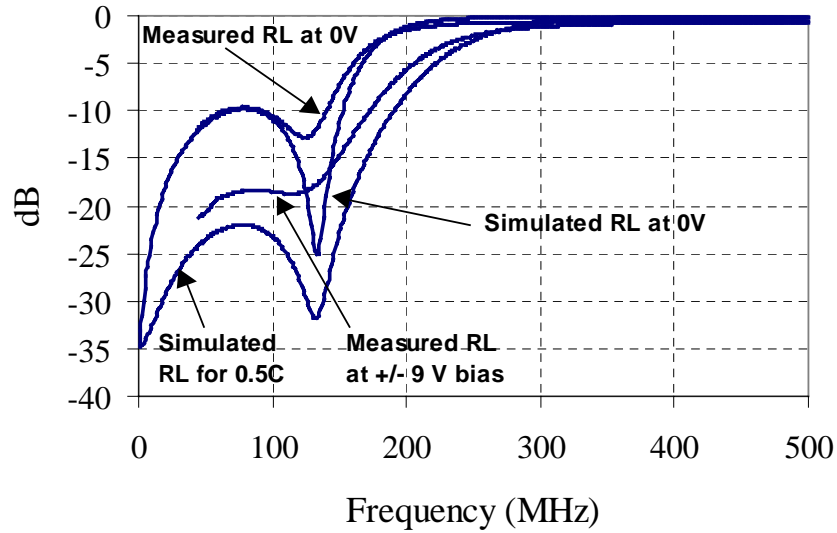
Figure 5.3: Simulated and measured return loss of the tunable LPF.

The filter mentioned herein is the first demonstration of a BST capacitor based lowpass filter. Research on construction of higher order lowpass filters (for better stopband attenuation characteristics) still continues.

An important measure of a tunable filter is the intermodulation distortion (IMD) generated. In the following sub-chapter, a discussion will be made on IMD generated in BST capacitor based tunable lowpass filters.

5.2.1 Intermodulation Distortion in Tunable LPFs

Intermodulation distortion (IMD) is a measure of the linearity of a two port nonlinear circuit and sets the dynamic range of the device. When two signals at frequencies f_1 and f_2 MHz, which are very close to each other, are injected to a nonlinear two port circuit, harmonics of the fundamental signals and their cross products are generated. Of particular interest are the 3rd order products at $2f_1$-f_2 and $2f_2$-f_1. This is a troublesome effect in RF systems. If a weak signal accompanied by two strong interferers experiences third order nonlinearity, then one of the IMD products falls in the band of interest, corrupting the desired component. The corruption of signals due to 3rd order products of two nearby interferers is so common and so critical that a performance metric has been defined to characterize this behavior. Called the 3rd order intercept point (IP3), this parameter can be measured by a two-tone test as in Figure 5.4.
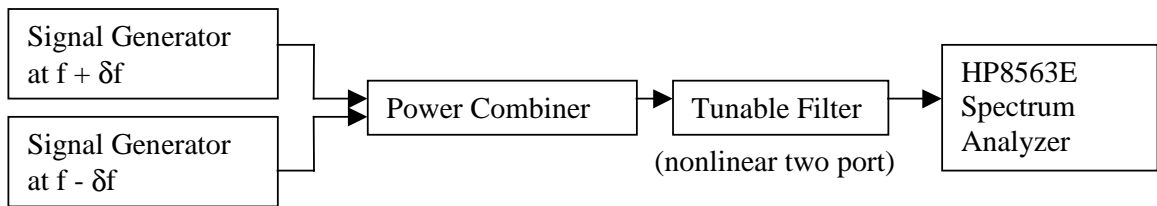
Figure 5.4: Measurement setup for the intermodulation distortion.

A spectrum similar to Figure 5.5 is observed in the spectrum analyzer. In this spectrum, increasing the input power raises the fundamental signal's power by one time,

whereas it increases the 3rd order product's power by three times. IP3 is theoretically defined as the level of the output power (or input power) at which the fundamental signal's power and the 3rd order product's power are equal to each other, and can be calculated using the formula below.

$$Ouput\ IP3 = P_{fund} + \frac{P_{fund} - P_{3rd}}{2} \qquad (5.3)$$
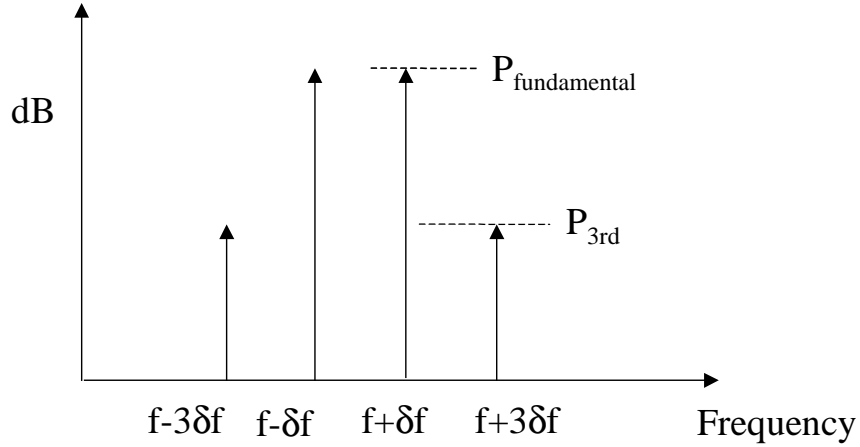
Figure 5.5: Spectrum observed in the spectrum analyzer.

The IMD measurements were performed based on the lowpass filter given in Figure 5.3. The output 3rd order intercept point (IP3) measurement results along with the IP3 simulation results can be seen in Figure 5.6. The small signal tunability curve of the BST sample used in this lowpass filter was fit to a polynomial based nonlinear capacitor. Also, the current flowing through the BST capacitor with the applied DC voltage was measured with a picoamp ammeter. Then, the current vs. voltage relationship was fit to a nonlinear resistor model. Using the nonlinear capacitor and the nonlinear resistor obtained, a *Harmonic Balance (HB)* simulation was performed in HP-ADS and the expected output IP3 points were obtained (Figure 5.6). The BST capacitor's small signal tunability curve, and the measured current vs. voltage relationship can be seen in Figure 5.7 and Figure 5.8, respectively.
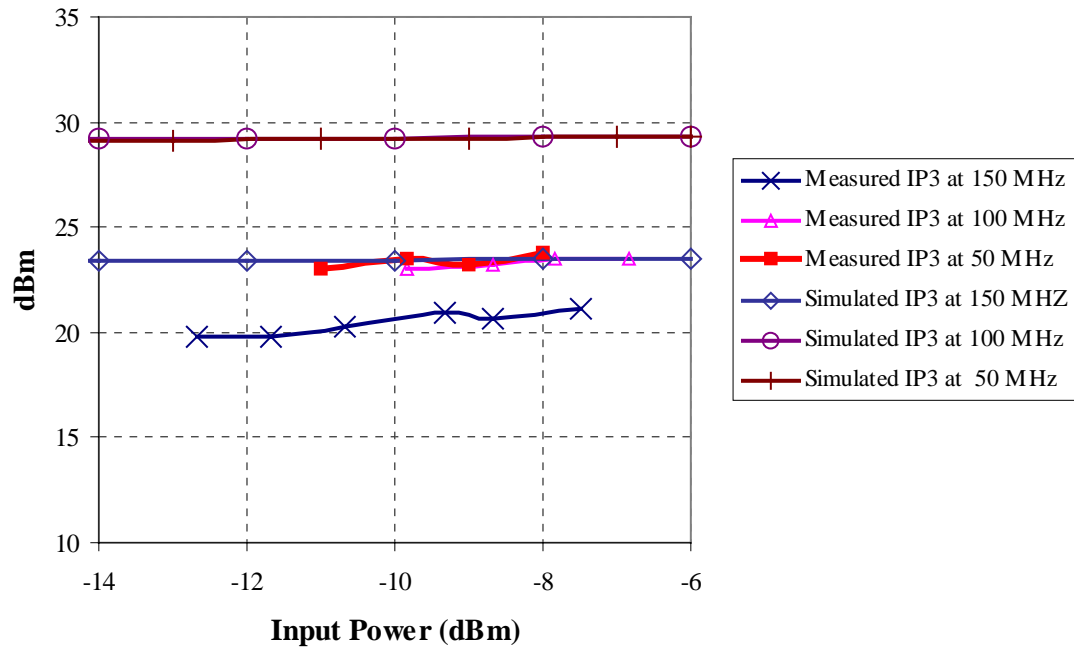
Figure 5.6: Measured and simulated IP3.
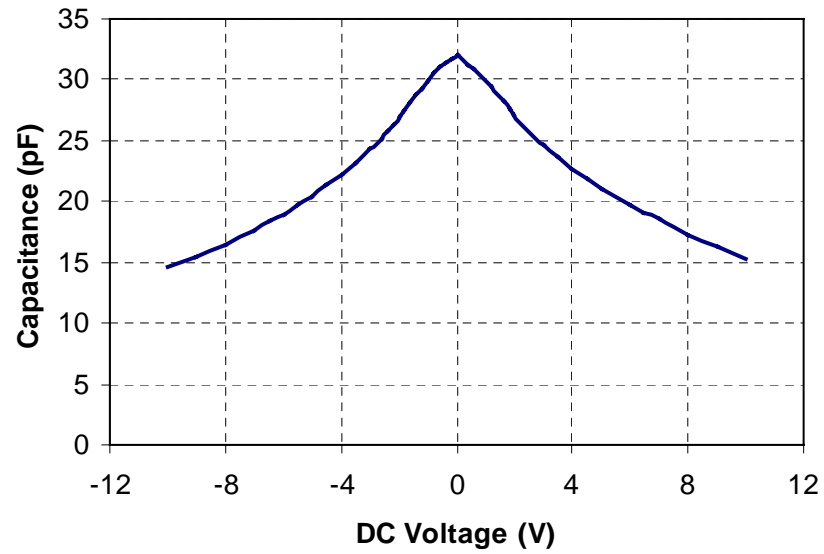
Figure 5.7: Small signal tunability curve of the BST capacitor used in the filter.
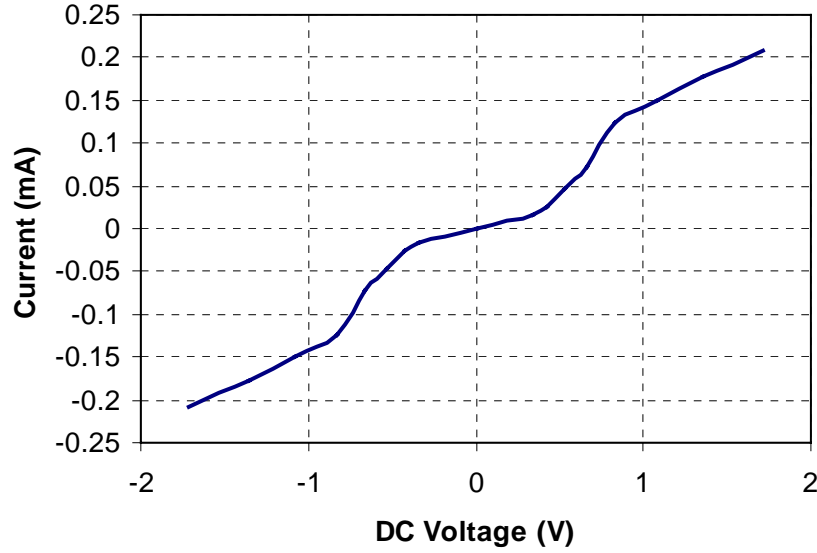
Figure 5.8: Current vs. voltage curve of the BST capacitor.

It can be seen from Figure 5.6 that the IP3 near the cut-off frequency drops. This is evident from the fact that near cut-off, more RF voltage drops on the BST capacitors, thus resulting in increased level of harmonics generated and less IP3 measured. There is a discrepancy between simulated and measured IP3. The research characterizing this discrepancy is still underway.

5.3. Tunable Bandpass Filters Using BST

Another filter type which can be implemented by using BST capacitors is a bandpass filter (BPF) shown in Figure 5.9. However, fabrication of this topology is practically very difficult, because connecting a tunable BST capacitor in the series path requires an isolated ground for the capacitors, and it is physically very hard to construct using the available capacitor substrates (refer to Figure 4.2). However, the series LC circuit in Figure 5.9 can be converted to a parallel LC circuit by using impedance inverters seen in Figure 5.10 [29], resulting in a circuit which is easier to fabricate.
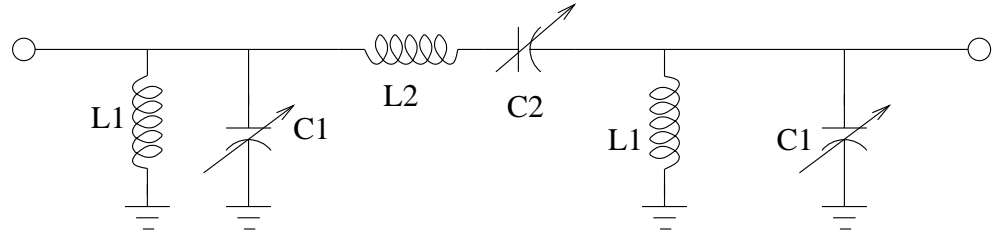
Figure 5.9: Schematics of a 3rd order tunable BPF.
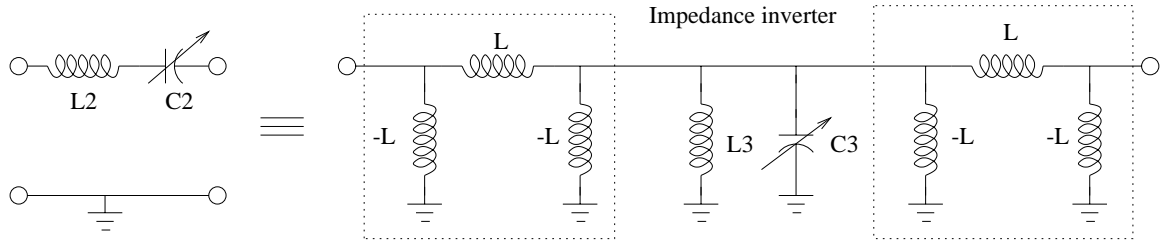
Figure 5.10: Inversion of series LC to parallel LC.

Note that inductors provide a DC short to the ground, thus making it impossible to apply the tuning DC bias to the filter. One possible solution involves connecting a very large capacitor in series with the BST capacitors thus providing a DC isolation for the capacitors. An alternate and easier solution is to connect a very large capacitor in series with the inductors, L_{11} and L_{22}, as shown in Figure 5.11, preventing them from shorting the DC tuning voltage. The complete circuit for the filter then can be seen in Figure 5.11.
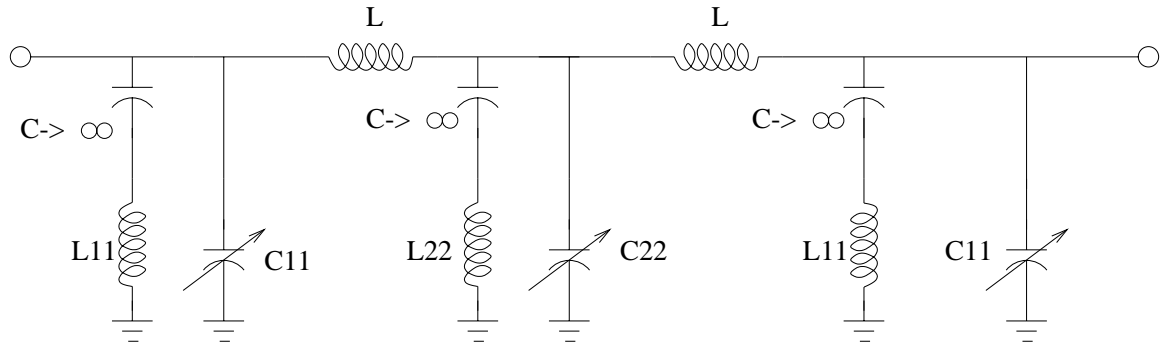
Figure 5.11: The complete circuit of the proposed filter.

Based on the available BST capacitors, the BPF in Fig.11 was designed with the component values; L=47 nH, L_{11}=11 nH, L_{22}=15 nH, and $C_{11}=C_{22}$=95 pF. The simulation results for this design are shown in Figure 5.12. The results show that the 3-dB center frequency of the BPF can be tuned from 167 MHz to 236 MHz, resulting in 41 % tunability by halving the value of the BST capacitors. Also, the insertion loss in the passband is better than 0.44 dB while the return loss is better than 10 dB. Fabrication of this bandpass filter will be the subject of future work.
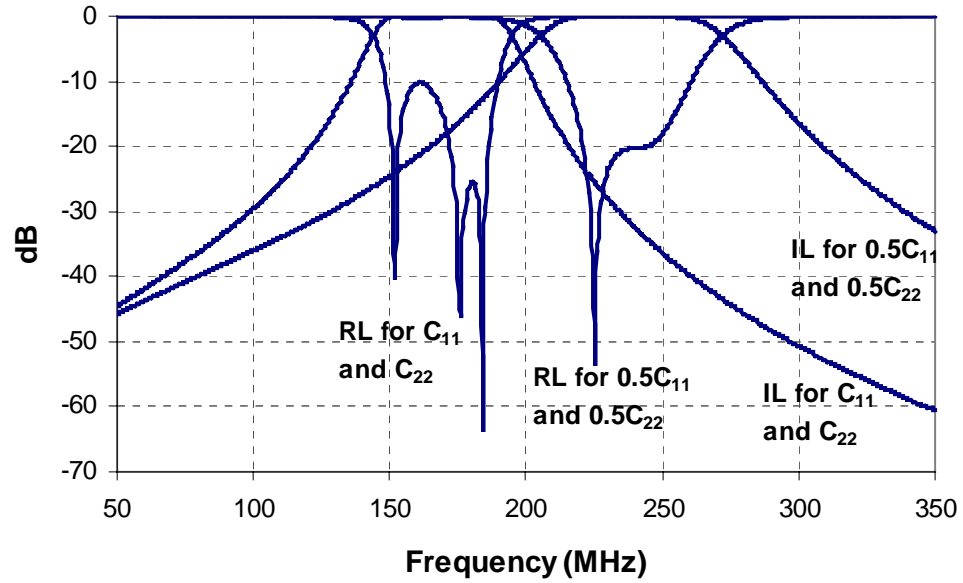
Figure 5.12: Simulated response of the tunable BPF.

Chapter 6

BST Phase Shifters

6.1. Introduction

Phased array antennas can steer transmitted and received signals without mechanically rotating the antenna. Each radiating element of a phased array is usually connected to a phase shifter and a driver, which determine the phase of the signal at each element to form a beam at the desired angle. The most commonly used phase shifters are ferrite and semiconductor based phase shifters. Ferrite phase shifters are very slow to respond to control voltages, whereas semiconductor based phase shifters are much faster, but they suffer from high losses at microwave frequencies and have limited power handling capabilities. On the other hand, ferroelectric based phase shifters offer a variety of benefits to resolve these difficulties [22].

In this section, the design methodology of a loaded line phase shifter will be discussed. The contribution of conductor losses and BST losses will be identified through several simulations. This will allow to investigate the influence of the loss tangent of BST and the properties of the conductor on the insertion loss of the phase shifter.

6.2. Phase Shifter Design

A periodically loaded line phase shifter has been reported to have several advantages over previously reported phase shifters, such as promising loss performance,

moderate control voltages, and compatibility with monolithic fabrication techniques. It utilizes a high impedance transmission line which is loaded periodically by the BST varactors (Figure 6.1). The high impedance transmission line can be approximated in terms of its inductance per unit length (L_t), and capacitance per unit length (C_t) at frequencies well below the cut-off frequency (Bragg frequency) that the approximate circuit represents [30] (Figure 6.2). The capacitance per unit length of the loaded transmission line can be controlled by applying a voltage to the BST capacitors, so the characteristic impedance and the phase velocity of the loaded line can be changed electronically.
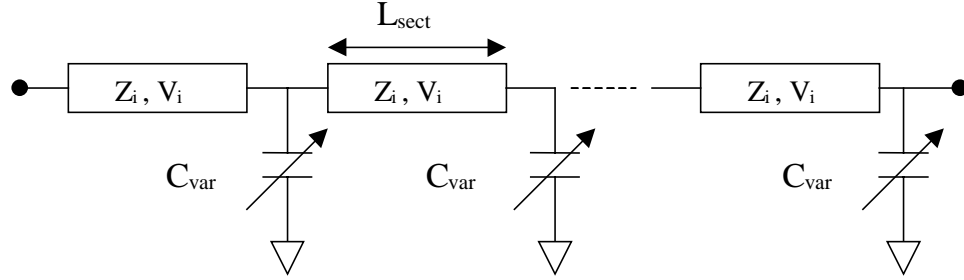
Figure 6.1: Schematic illustration of a periodically loaded phase shifter.
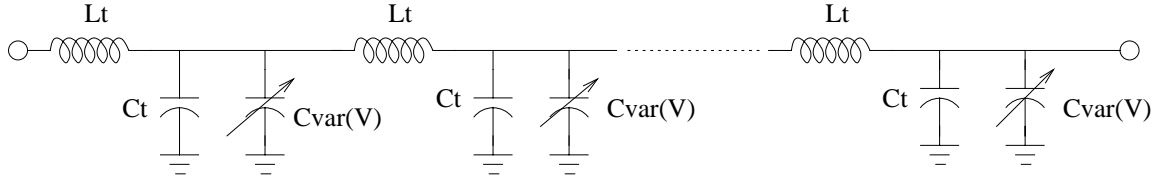
Figure 6.2: Approximate circuit for the BST varactor loaded transmission line.

The phase shifter was intended to give 360^0 phase shift at 20 GHz, so the Bragg frequency was chosen as 40 GHz for the design. The BST capacitors were assumed to have a tunability of 2:1 (50%). The characteristic impedance of the unloaded transmission line is given by [23],

$$Z_i = 50\sqrt{1+x} \qquad (6.1)$$

where x is the loading ratio defined as,

$$x = \frac{C_{var}^{max}/L_{sect}}{C_t} \qquad (6.2)$$

where C_{var}^{max} is the 0 V bias capacitance of the loading BST capacitors, and L$_{sect}$ is the length of one unit cell.

The capacitance per unit length of a transmission line can be expressed in terms of its characteristic impedance and the phase velocity by:

$$C_t = \frac{1}{Z_i \cdot v_i} \qquad (6.3).$$

Using (6.2) and (6.3) C$_{var}$^{max} can be derived as:

$$C_{var}^{max} = x\frac{L_{sect}}{Z_i \cdot v_i} \qquad (6.4).$$

In [23], the ratio of L$_{sect}$ to the phase velocity of the unloaded transmission line, v_i, was derived as:

$$\frac{L_{sect}}{v_i} = \frac{1}{\pi \cdot f_{Bragg}^{min}\sqrt{1+x}} \qquad (6.5).$$

The design used here consists of a coplanar waveguide (CPW) of characteristic impedance Z$_i$=74 Ω (x=1.2), loaded periodically with BST capacitors whose zero bias capacitance is 87 fF. After capacitive loading, the characteristic impedance of the loaded line reduces to 50 Ω. The substrate of the transmission line is silicon, whose dielectric constant is 11.8. The required characteristic impedance of the line was designed in the Agilent ADS-LineCalc program resulting in a width, W, and gap, G, of 100 μm and 225 μm, respectively. The phase velocity in this structure will be v_i =1.2x10^8 m/s. Using (6.5), L$_{sect}$ can be calculated as 640 μm. The phase shift from a single section was given in [23] as:

$$\Delta\vartheta = 360f\,\frac{L_{\text{sect}}}{\upsilon_i}\left(\sqrt{1+x} - \sqrt{1+\frac{x}{2}}\,\right) \qquad (6.6).$$

Using (6.6), the phase shift per unit section can be calculated as 8.4^0. In order to obtain a phase shift of 360^0 at 20 GHz, 42 identical cells are connected in series resulting in a total length of 2.7 cm. The structure in Figure 6.3 describes the circuit designed.
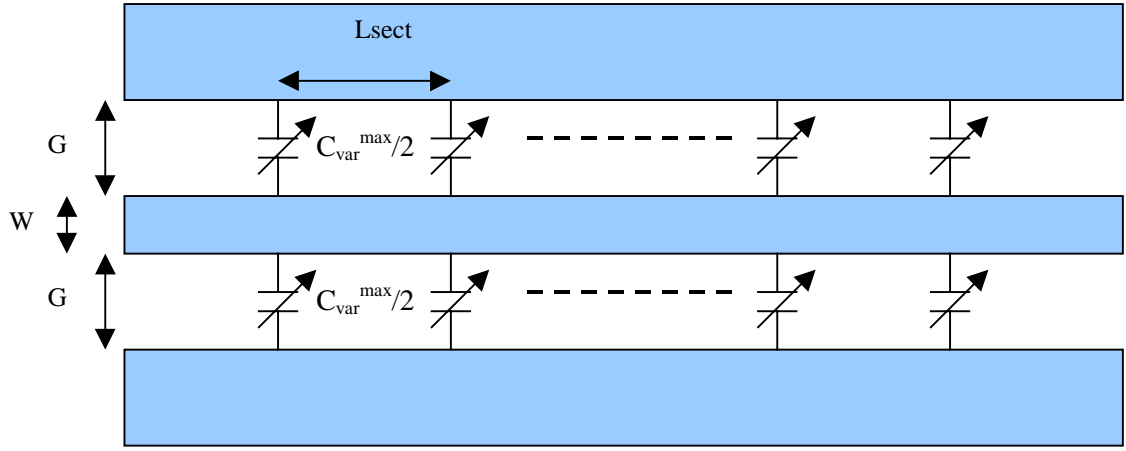
Figure 6.3: Structure of the phase shifter.

6.3. Simulation Results

The phase shifter circuit was simulated in HP-ADS. In the simulation, the ADS CPW model along with the ADS "capacitor with Q" model was used. The details of the circuit setup is shown in Appendix E. Through these simulations, the effects of the loss tangent (1/Q) of the BST capacitors, conductivity and the thickness of the conductor on the insertion loss of the phase shifter were analyzed. The phase shift obtained from changing the values of the loading capacitance is plotted in Figure 6.4. It is possible to obtain a phase shift of 379° at 20GHz. The small deviation from the designed value is due to the limits of the approximate circuit of Figure 6.2 as the frequency approaches to the Bragg frequency.
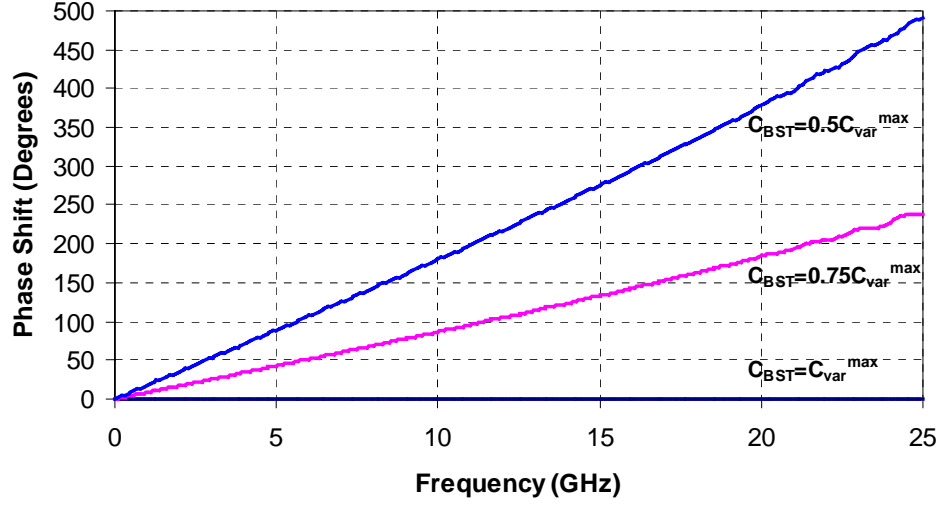
Figure 6.4: Simulated phase shift as loading capacitance changes.

The insertion loss and return loss of the circuit (without including the conductor losses and the BST losses) are shown in Figure 6.5 and Figure 6.6, respectively. The insertion loss of the phase shifter (due to the impedance mismatch) is lower than 0.1 dB, while the return loss is better than 15 dB for all loading conditions.
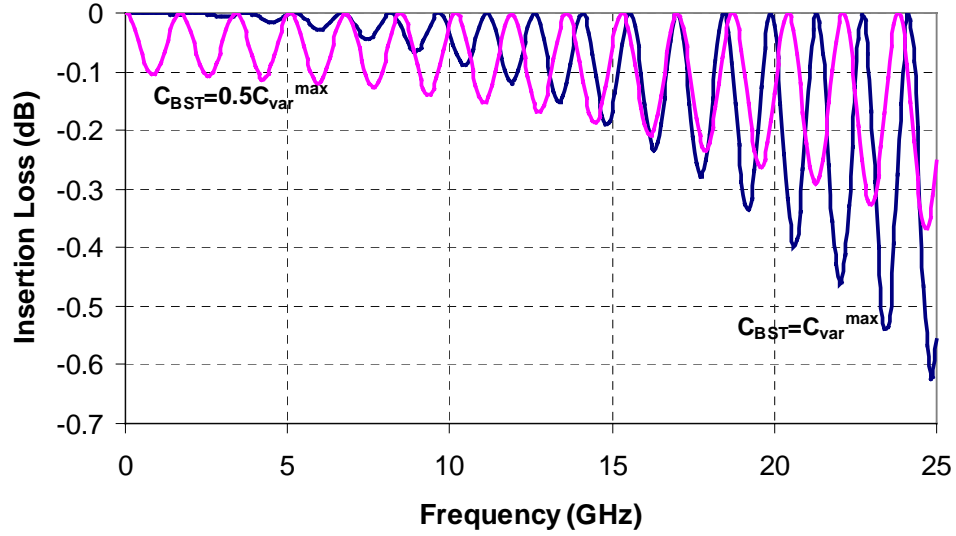
Figure 6.5: Insertion loss of the phase shifter as loading capacitance changes.
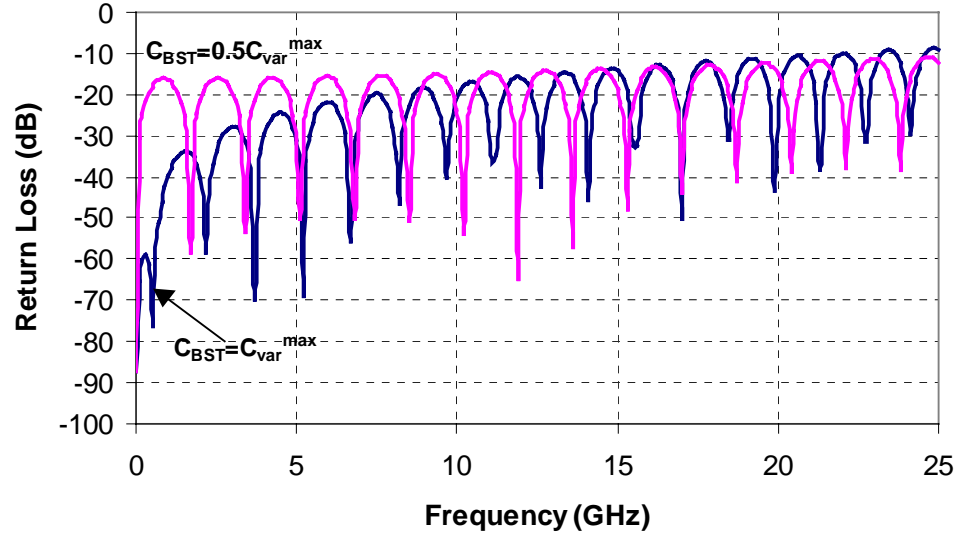
Figure 6.6: Return loss of the phase shifter as loading capacitance changes.

Also, the insertion loss of the circuit was simulated for several different metal types, conductor thickness values, and loss tangents of BST. The simulation results can be seen in Figure 6.7, Figure 6.8 and Figure 6.9, respectively.
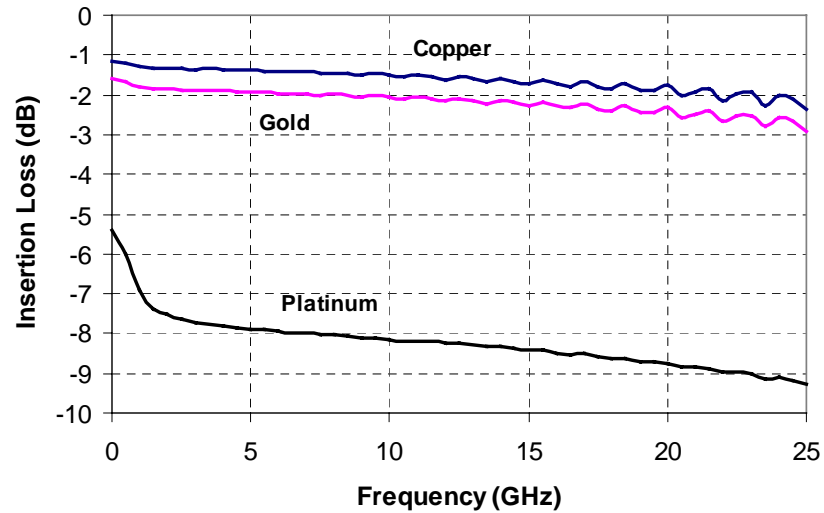
Figure 6.7: Insertion loss of the phase shifter for different metals (Thickness of the metal is assumed 1 μm and the BST capacitors have no loss).
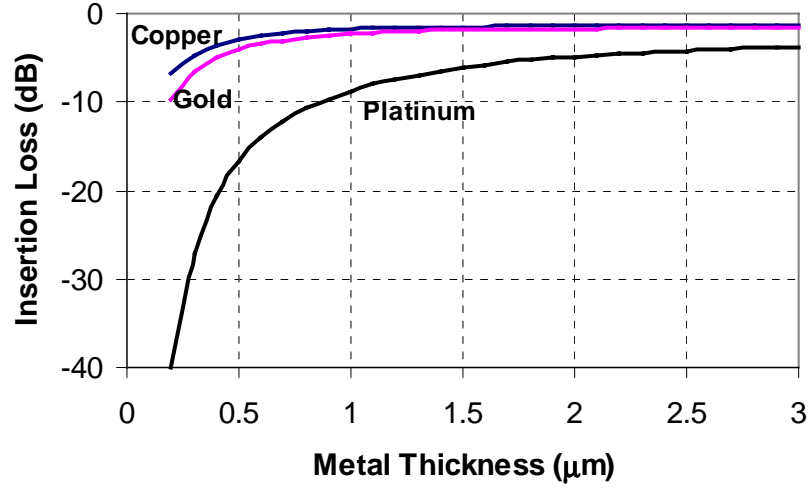
Figure 6.8: Insertion loss vs. conductor thickness at f=20 GHz.
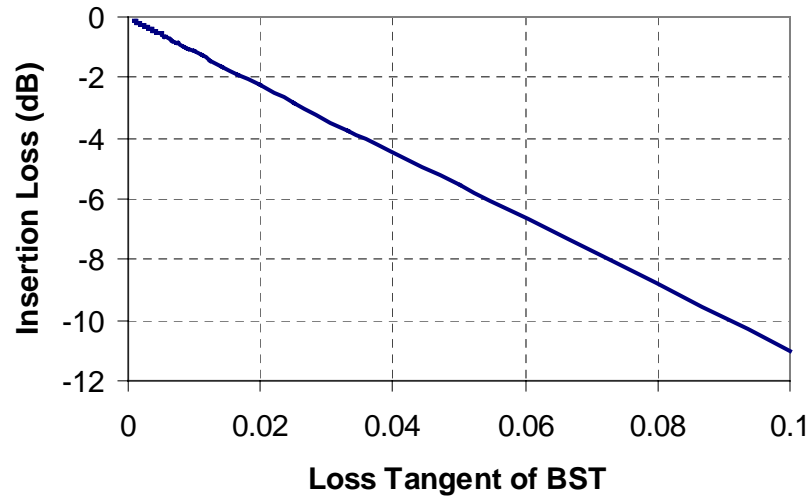
Figure 6.9: Insertion loss vs. the loss tangent of BST (f=20 GHz, no conductor loss).

From the simulations, it can be concluded that the conductor type and its thickness have a major impact on the insertion loss of the phase shifter. More attention should be paid to obtain thicker metals. The conductor thickness can be increased up to

the skin depth to provide better insertion loss characteristics. Using copper or gold as conductor greatly improves the insertion loss of the phase shifter. However, it is very difficult to process BST and copper (or gold) together, whereas platinum is easier to work with [1]. Furthermore, it can be seen from Figure 6.9 that obtaining low loss BST (tan$\delta \leq$ 0.007-0.008) is required for BST phase shifters to be a substitute for semiconductor based phase shifters. In this case, the contribution of BST losses on the insertion loss becomes approximately one third of the contribution of diode losses in a semiconductor based phase shifter (similar to [23]).

Chapter 7

Conclusions and Future Work

7.1. Conclusions

Parallel plate capacitors fabricated on MOCVD grown BST thin films have yielded a typical tuning range of 4.18:1 (76 %) and a typical loss tangent of 0.003 at VHF frequencies. The dielectric constant of BST has been shown to be constant up to microwave frequencies. The measured total quality factor of a 31 pF BST capacitor was 70 at 45 MHz. This result favorably compares with commercially available varactor diodes (such as M/ACOM #MA4ST079) and it shows that BST capacitors are promising substitutes for varactors diodes. Furthermore, the effect of large RF signal amplitudes on the tunability of the capacitors was studied. Increasing the RF level across the BST capacitors decreases the tunability. This effect needs to be considered for applications where a large RF signal across a BST capacitor is present. A nonlinear circuit model based on the measurements was developed for the BST capacitors. This model will help the designer to predict the nonlinear properties of future BST based circuits.

One of the applications of BST includes the design of tunable filters. A BST capacitor based 3rd order tunable lowpass filter was demonstrated for the first time. The filter showed good agreement between measured and simulated responses. Also, the intermodulation distortion generated by the filter was measured and simulated by a nonlinear model for the BST capacitor. A bandpass filter utilizing impedance inverters

was designed. Approximately 40 % tunability in frequency is achievable by halving the BST capacitors.

Another important application of BST is a phase shifter. A distributed phase shifter periodically loaded with BST capacitors was designed and several simulations were performed to determine the contribution of conductor losses and BST losses. Conductor type and its thickness have a major impact on the insertion loss of the phase shifter. More attention is needed for obtaining conductor thicknesses near to skin depth. Obtaining low loss BST (tan$\delta \leq$ 0.007-0.008) is required for BST phase shifters to be a viable substitute for semiconductor based phase shifters, in which the contribution of BST losses on the insertion loss becomes approximately one third of the contribution of diode losses.

7.2. Future Work

Intended goals include the complete characterization of BST capacitors such that the large signal effects and the intermodulation distortion generated can be accurately predicted. This requires precise measurement systems and better models for the BST capacitors. Furthermore, the designed phase shifter and tunable bandpass filter will be fabricated in the near future. Incorporation of BST in some other applications (such as voltage controlled oscillators and tunable matching networks) will also be studied.

Bibliography

[1] Tombak, A.; Ayguavives F. T.; Maria, J.-P.; Stauf, G.T.; Kingon, A.I.; Mortazawi, A., "Low voltage tunable barium strontium titanate thin film capacitors for RF and microwave applications", *Microwave Symposium Digest. 2000 IEEE MTT-S International Conference*, pp: 1345 – 1348, June 11-16, 2000, Vol.3.

[2] Miranda, F.A.; Mueller, C.H.; Cubbage, C.D.; Bhasin, K.B.; Singh, R.K.; Harkness, S.D., "HTS/ferroelectric thin films for tunable microwave components", *IEEE Transactions on Applied Superconductivity,* Volume: 5 2 3 , June 1995 , pp: 3191-3194.

[3] De Flaviis, F.; Alexopoulos, N.G.; Stafsudd, O.M., "Planar microwave integrated phase-shifter design with high purity ferroelectric material", *IEEE Transactions on Microwave Theory and Techniques,* Volume: 45 6 , June 1997 , pp: 963 –969.

[4] De Flaviis, F.; Chang D.; Alexopoulos, N.G.; Stafsudd, O.M, "High Purity Ferroelectric Materials by sol-Gel Process for Microwave Applications", 1996 *IEEE MTT-S Digest.*

[5] S K Streiffer; C Basceri; C B Parker; S E Lash and A I Kingon, "Ferroelectricity in Thin Films: The Dielectric Response of Fiber-Textured $(Ba_xSr_{1-x})Ti_{1+y}O_{3+z}$ Thin Films Grown by Chemical Vapor Deposition", *J Appl. Phys.*, Vol.86[8] pp: 4565-4575, 1999.

[6] Kim, H. G., "Research overview and application trend in ferroelectric thin films", *Proceedings of the 5th International Conference on properties and Applications of Dielectric Materials*, 1997, Volume: 2 , 1997 pp: 990 -994 Vol.2.

[7] Tang, K.S.; Lau, W.S.; Samudra, G.S., "Trends in DRAM dielectrics *", IEEE Circuits and Devices Magazine* , Volume: 13 Issue: 3 , May 1997, pp: 27 -34

[8] Kozyrev, A.; Ivanov, A.; Keis, V.; Khazov, M.; Osadchy, V.; Samoilova, T.; Soldatenkov, O.; Pavlov, A.; Koepf, G.; Mueller, C.; Galt, D.; Rivkin, T., "Ferroelectric films: nonlinear properties and applications in microwave devices", *1998 IEEE MTT-S International Microwave Symposium Digest*, Volume: 2 , 1998 pp: 985 -988 vol.2.

[9] Kingon, A. I.; Auciello O., "A critical review of physical vapor deposition techniques for the synthesis of ferroelectric thin films", *Proceedings of the Eighth IEEE International Symposium on Applications of Ferroelectrics*, 1992. ISAF '92., pp: 320 – 331.
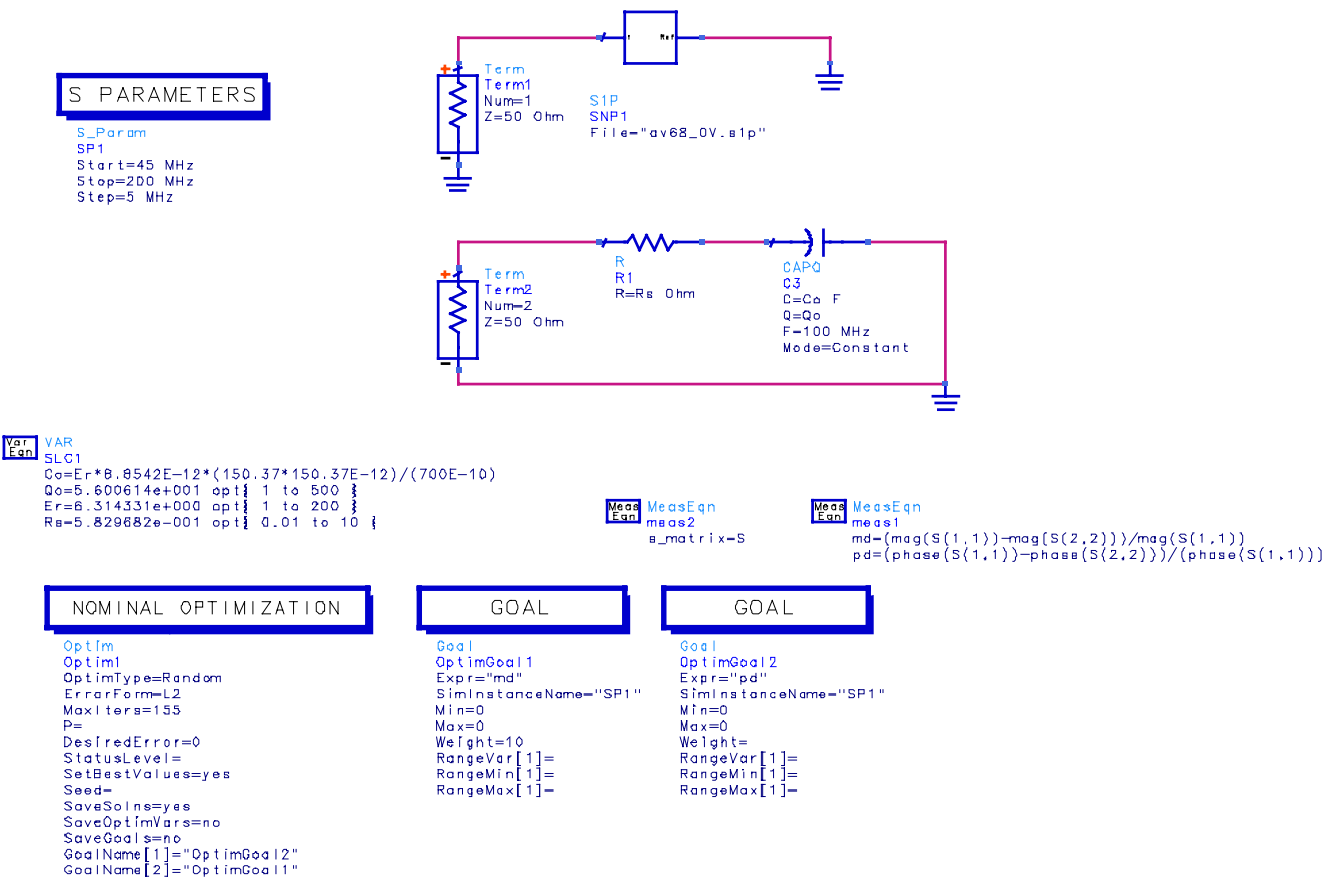
[10] Streiffer, S.K.; Basceri, C.; Parker, C.B.; Lash, S.E.; Christman, J.; Maiwa, H.; Kingon, A.I, "The influence of strain on the dielectric behavior of $(Ba_xSr_{1-x})Ti_{1+y}O_{3+z}$ thin films grown by LS-MOCVD on $Pt/SiO_2/Si$", *Proceedings of the Eleventh IEEE International Symposium on Applications of Ferroelectrics*, 1998. ISAF 98., pp: 31 – 34.

[11] Raymond, M. V.; Al-Shareef H. N.; Dimos D. B.; Missert N.; Mueler C. H.; Galt D., "Sputter deposition of $SrTiO_3$ thin films for voltage tunable capacitors", *Integrated Ferroelectrics*, 1997, Vol.17 pp:247-256.

[12] Kozyrev A. B.; Hollmann E. K.; Ivanov A. V.; Soldatenkov O. I., "Microwave properties of $Yba_2Cu_3O_{7-x}/SrTiO_3$ Planar Capacitors", *Integrated Ferroelectrics*, 1997, Vol.17, pp:257-262.

[13] Kozyrev A. B.; Samoilova T. B.; Golovkov A. A.; Hollmann E. K.; Kalinikos D. A.; Loginov V. E.; Prudan A. M.; Soldatenkov O. I.; Mueller C. H.; Rivkin T. V.; Koepf G. A., "Nonlinear properties of $SrTiO_3$ films at microwave frequencies", *Integrated Ferroelectrics*, 1997, Vol. 17, pp:263-271.

[14] Galt, D.; Price, J.C.; Beall, J.A.; Harvey, T.E., "Ferroelectric thin film characterization using superconducting microstrip resonators", *IEEE Transactions on Applied Superconductivity*, Volume: 5 Issue: 2 Part: 3 , June 1995 pp: 2575 –2578

[15] Treece, R.E.; Thompson, J.B.; Mueller, C.H.; Rivkin, T.; Cromar, M.W., "Optimization of $SrTiO_3$ for applications in tunable resonant circuits", *IEEE Transactions on Applied Superconductivity*, Volume: 7 Issue: 2 Part: 3 , June 1997 pp: 3512 –3515.

[16] Stauf, G.T.; Bilodeau, S.; Watts, R.K., "$BaSrTiO_3$ thin films for integrated high frequency capacitors", 1996. ISAF '96, *Proceedings of the Tenth IEEE International Symposium on Applications of Ferroelectrics*, pp: 103 - 106 vol.1.

[17] J. M. Pond; S. W. Kirchoefer; W. Chang; J. S. Horwitz; and D. B. Chrisey, "Microwave Properties of Ferroelectric Thin Films", *Integrated Ferroelectrics*, 1998, Vol.22, pp:317-328.

[18] J. S. Horwitz; W. Chang; A. C. Carter; J. M. Pond; S. W. Kirchoeffer; D. B. Chrisey; J. Levy and C. Hubert, "Structure Relationships in Ferroelectric Thin films for Frequency Agile Microwave Electronics", *Integrated Ferroelectrics*, 1998, Vol 22, pp: 279-289.

[19] F. Hui; Z. Chen; K. Shen; J. Lau; M. Huang; M. Chan; P. K. Ko; G. Jin; P. C. H. Chan, "High-Q SOI Gated Varactor for use in RFICs", *Proceedings of 1998 IEEE International SOI Conference*, Oct. 1998.

[20] Subramanyam, G.; Van Keuls, F.; Miranda, F.A., "A K-band tunable microstrip bandpass filter using a thin-film conductor/ferroelectric/dielectric multilayer

configuration", *IEEE Microwave and Guided Wave Letters*, pp: 78 – 80, Feb. 1998, Vol.8, Issue.2.

[21] Subramanyam, G.; Van Keuls, F.; Miranda, F.A., "A K-band frequency agile microstrip bandpass filter using a thin-film HTS/ferroelectric/dielectric multilayer configuration", *IEEE Transactions on Microwave Theory and Techniques,* pp: 525-530, April 2000 vol.48,. Issue.4, Part.1.

[22] Erker, E.G.; Nagra, A.S.; Yu Liu; Periaswamy, P.; Taylor, T.R.; Speck, J.; York, R.A., "Monolithic Ka-band phase shifter using voltage tunable $BaSrTiO_3$ parallel plate capacitors", *IEEE Microwave and Guided Wave Letters*, Volume: 10 1 , Jan. 2000 , pp: 10 –12.

[23] Nagra, A.S.; York, R.A., "Distributed analog phase shifters with low insertion loss", *IEEE Transactions on Microwave Theory and Techniques*, Volume: 47 9 1 , Sept. 1999 , pp: 1705 –1711.

[24] S. K. Streiffer; C. Basceri; A. I. Kingon; S. Lipa; S. Bilodeau; R. Carl and P. C. Van Buskirk, "Dielectric behavior of CVD $(Ba,Sr)TiO_3$ thin films on Pt/Si", *Proceedings of the Fall 1995 Material Research Society (MRS) Conference, Boston, MA, December.*

[25] Alluri P.; Gao Y. and Tran T., "Isotopic study of metalorganic chemical vapor deposition of $(Ba, Sr)TiO_3$ films on Pt", *Applied Physics Letters* - July 19, 1999 -- Volume 75, Issue 3, pp: 415-417.

[26] C. Basceri; S.E. Lash; C.B. Parker; S.K. Streiffer; A.I. Kingon; M. Grossmann; S. Hoffmann; M. Schumacher; R. Waser; S. Bilodeau; R. Carl; P.C. van Buskirk and S.R. Summerfelt, "An Important Failure Mechanism in MOCVD $(Ba,Sr)TiO_3$ Thin Films: Resistance Degradation", *Proceedings of the Materials Research Society*, Vol 493 (Ferroelectric Thin Films VI), 9 - 14 (1998)).

[27] Tung-Sheng Chen; Balu, V.; Katakam, S.; Jian-Hung Lee; Lee, J.C., "Effects of Ir electrodes on barium strontium titanate thin-film capacitors for high-density memory application", *IEEE Transactions on Electron Devices*, pp: 2304 – 2310, Dec 1999, Vol.46, Issue.12.

[28] Uher J.; Hoefer W. J. R., "Tunable microwave and millimeter-wave band-pass filters", *IEEE Transactions on Microwave Theory and Techniques*, pp: 643-653, April 1991, Vol.39, Issue:4.

[29] Matthaei G. L.; Young L.; Jones E. M. T., Microwave filters, Impedance-Matching Networks, and Coupling Systems, Artech House Inc., 1980, pp: 434-438.

[30] M. J. W. Rodwell; S. T. Allen; R. Y. Yu; M. G. Case; U. Bhattacharya; M. Reddy; E. Carman; M. Kamegawa; Y. Konishi; J. Pusl; R. Pullela; and J. Esch, "Active and nonlinear wave propagation devices in ultrafast electronics and optoelectronics," *Proceedings of IEEE*, Vol. 82, pp: 1035–1059, July 1994.

Appendix A

Simulation Setup used in Optimization

S PARAMETERS

S_Param
SP1
Start=45 MHz
Stop=200 MHz
Step=5 MHz

Term
Term1
Num=1
Z=50 Ohm

S1P
SNP1
File="av68_0V.s1p"

R
R1
R=Rs Ohm

CAPQ
C3
C=Co F
Q=Qo
F=100 MHz
Mode=Constant

Term
Term2
Num=2
Z=50 Ohm

VAR
SLC1
Co=Er*8.8542E-12*(150.37*150.37E-12)/(700E-10)
Qo=5.600614e+001 opt{ 1 to 500 }
Er=6.314331e+000 opt{ 1 to 200 }
Rs=5.829682e-001 opt{ 0.01 to 10 }

MeasEqn
meas2
a_matrix=S

MeasEqn
meas1
md=(mag(S(1,1))-mag(S(2,2)))/mag(S(1,1))
pd=(phase(S(1,1))-phase(S(2,2)))/(phase(S(1,1)))

NOMINAL OPTIMIZATION

Optim
Optim1
OptimType=Random
ErrorForm=L2
MaxIters=155
P=
DesiredError=0
StatusLevel=
SetBestValues=yes
Seed=
SaveSolns=yes
SaveOptimVars=no
SaveGoals=no
GoalName[1]="OptimGoal2"
GoalName[2]="OptimGoal1"

GOAL

Goal
OptimGoal1
Expr="md"
SimInstanceName="SP1"
Min=0
Max=0
Weight=10
RangeVar[1]=
RangeMin[1]=
RangeMax[1]=

GOAL

Goal
OptimGoal2
Expr="pd"
SimInstanceName="SP1"
Min=0
Max=0
Weight=
RangeVar[1]=
RangeMin[1]=
RangeMax[1]=

Appendix B

Basics of Short-Open-Load Reflection Calibration

In this section, the SOL reflection calibration algorithm will be discussed. In a network analyzer measurement system, the actual data measured at the DUT and read at the network analyzer differs dramatically due to the line losses and phase differences in the connections. This requires correction for the errors (the middle box in Figure B.1.) which are assumed to be linear.
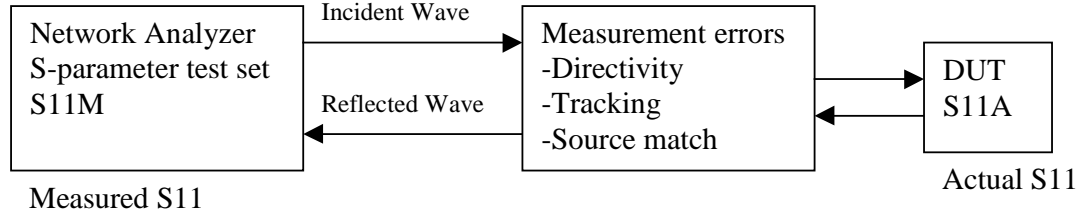

Figure B.1: A reflection measurement setup.

Let the s-parameters of the error network be:

$$S := \begin{bmatrix} e00 & e01 \\ e10 & e11 \end{bmatrix}$$ (B.1)

Then, the measured S-parameters at the network analyzer can be expressed in terms of S11A and S as:

$$S11M = e00 + \frac{(S11 \cdot e10 e01)}{(1 - e11 \cdot S11A)}$$ (B.2)

Therefore, replacing the DUT with open, short and load will return known reflection coefficients for S11A (Table B.1).

Table B.1: Reflection coefficients for the standards.

Standard	Reflection, S11A
50 Ω Load	S11AL = 0
Load	S11LS = -1
Open	S11AO = 1

$$S11ML = e00 + \frac{0 \cdot e01e10}{1 - e11 \cdot 0} \qquad (B.3)$$

$$S11MS = e00 + \frac{-1 \cdot e01e10}{1 - e11 \cdot (-1)} \qquad (B.4)$$

$$S11MO = e00 + \frac{1 \cdot e01e10}{1 - e11 \cdot (1)} \qquad (B.5)$$

Therefore, having three equations (B.3-B.5) and three unknowns (e00,e11,e01e10), it is possible to solve for e00, e11, and e01e10, and correct the measured S-parameters (S11M) to obtain the actual S-parameters (S11A).

Appendix C

Matlab Curvefitting Program

```
clear all;
format long g;

v=[-8 –7 –6 –5 –4 –3 –2 –1 0 1 2 3 4 5 6 7 8 ]';

Er=[174.4 182 195 207.6 223 242 257 279.4 308 308 286 260 237 217 199 185 173 ]';

degree=14;
coeff=polyfit(v,Er,degree);
coeff'
data1='';
for i=1:degree+1
   data=sprintf('%s%e*Eo,',data1,coeff(degree+2-i));
   data1=data;
end
data


x=linspace(-8,8,1400);
plot(x,polyval(coeff,x));
grid;
```
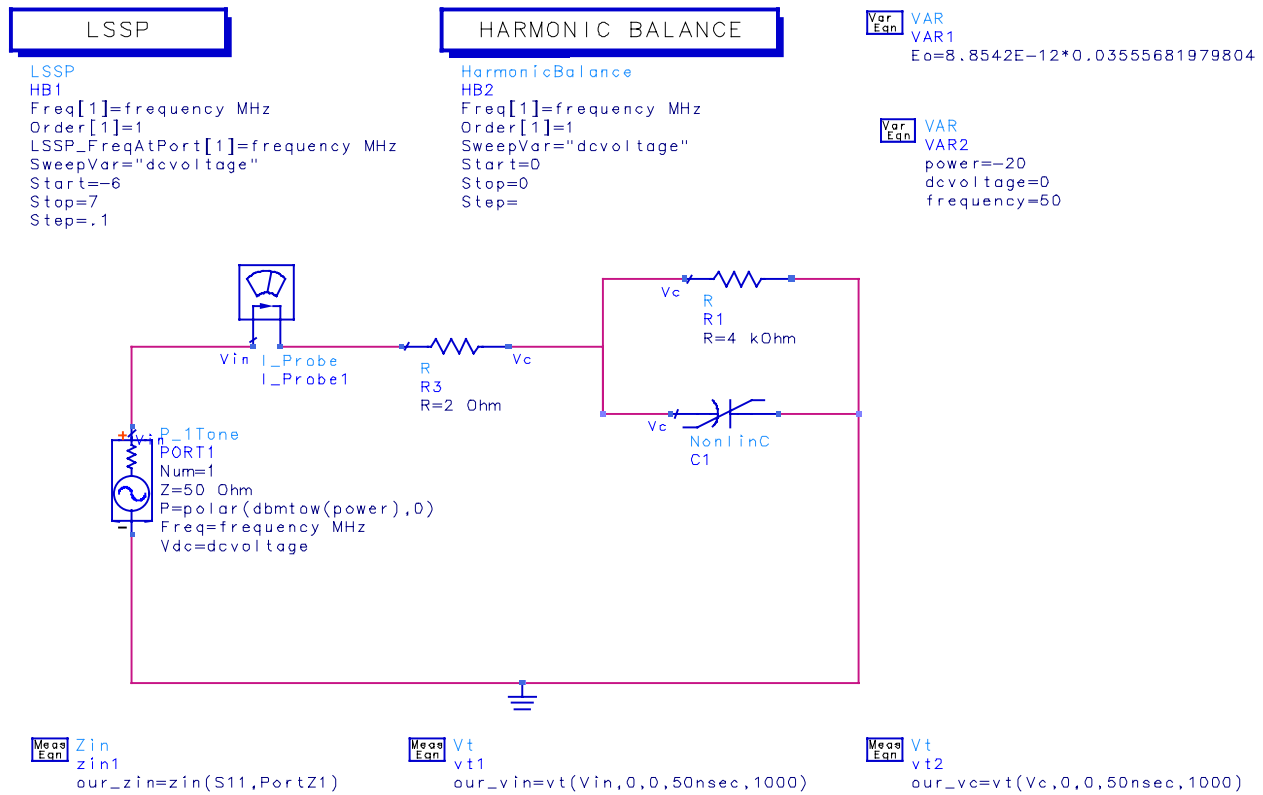
Appendix D

Large Signal S-Parameter Simulation Setup

```
LSSP

LSSP
HB1
Freq[1]=frequency MHz
Order[1]=1
LSSP_FreqAtPort[1]=frequency MHz
SweepVar="dcvoltage"
Start=-6
Stop=7
Step=.1
```

```
HARMONIC BALANCE

HarmonicBalance
HB2
Freq[1]=frequency MHz
Order[1]=1
SweepVar="dcvoltage"
Start=0
Stop=0
Step=
```

```
Var
Eqn  VAR
     VAR1
        Eo=8.8542E-12*0.03555681979804
```

```
Var
Eqn  VAR
     VAR2
        power=-20
        dcvoltage=0
        frequency=50
```

Vin I_Probe
I_Probe1

R
R3
R=2 Ohm

Vc

Vc
R
R1
R=4 kOhm

Vc
NonlinC
C1

P_1Tone
PORT1
Num=1
Z=50 Ohm
P=polar(dbmtow(power),0)
Freq=frequency MHz
Vdc=dcvoltage

```
Meas
Eqn  Zin
     zin1
        our_zin=zin(S11,PortZ1)
```

```
Meas
Eqn  Vt
     vt1
        our_vin=vt(Vin,0,0,50nsec,1000)
```

```
Meas
Eqn  Vt
     vt2
        our_vc=vt(Vc,0,0,50nsec,1000)
```

Appendix E

Simulation Setup of the Phase Shifter